Geophysical Journal International

Geophys. J. Int. (2021) **224,** 1753–1779
Advance Access publication 2020 August 31
GJI Seismology

doi: 10.1093/gji/ggaa412

Broad-band ground-motion simulation of 2016 Amatrice earthquake, Central Italy

Marta Pischiutta,[1] Aybige Akinci,[1] Elisa Tinti [1,2] and André Herrero[1]

[1] *Istituto Nazionale di Geofisica e Vulcanologia, Sezione Roma*1*, Via di Vigna Murata* 605*,* 00143 *Rome, Italy. E-mail: marta.pischiutta@ingv.it*
[2] *Dipartimento di Scienze della Terra, Università La Sapienza, Rome, Italy*

Accepted 2020 August 27. Received 2020 June 25; in original form 2020 February 4

SUMMARY

On 24 August 2016 at 01:36 UTC a M_L 6.0 earthquake struck several villages in central Italy, among which Accumoli, Amatrice and Arquata del Tronto. The earthquake was recorded by about 350 seismic stations, causing 299 fatalities and damage with macroseismic intensities up to 11. The maximum acceleration was observed at Amatrice station (AMT) reaching 916 cm s^{-2} on E–W component, with epicentral distance of 15 km and Joyner and Boore distance to the fault surface (R_{JB}) of less than a kilometre. Motivated by the high levels of observed ground motion and damage, we generate broad-band seismograms for engineering purposes by adopting a hybrid method. To infer the low frequency seismograms, we considered the kinematic slip model by Tinti *et al* . The high frequency seismograms were produced using a stochastic finite-fault model approach based on dynamic corner-frequency. Broad-band synthetic time-series were therefore obtained by merging the low and high frequency seismograms. Simulated hybrid ground motions were compared both with the observed ground motions and the ground-motion prediction equations (GMPEs), to explore their performance and to retrieve the region-specific parameters endorsed for the simulations. In the near-fault area we observed that hybrid simulations have a higher capability to detect near source effects and to reproduce the source complexity than the use of GMPEs. Indeed, the general good consistency found between synthetic and observed ground motion (both in the time and frequency domain), suggests that the use of regional-specific source scaling and attenuation parameters together with the source complexity in hybrid simulations improves ground motion estimations. To include the site effect in stochastic simulations at selected stations, we tested the use of amplification curves derived from HVRSs (horizontal-to-vertical response spectra) and from HVSRs (horizontal-to-vertical spectral ratios) rather than the use of generic curves according to NTC18 Italian seismic design code. We generally found a further reduction of residuals between observed and simulated both in terms of time histories and spectra.

Key words: Earthquake ground motions; Earthquake hazards; Seismic attenuation; Site effects.

1 INTRODUCTION

A M_w 6.0 earthquake occurred on 24 August 2016 at 3:36 am local time in central Italy, 1 km far from the Accumoli village and 9 km from the Amatrice town (latitude 42.70°, longitude 13.23°, depth 8.1 km, INGV-CNT Seismic Bulletin), according to the epicentral location led out through the Istituto Nazionale di Geofisica e Vulcanologia (INGV) seismic network (ISIDe 2016). The fault plane solution indicated normal faulting, according to the extensional tectonic regime in Central Apennines related to the opening of the Tyrrhenian back-arc basin, Fig. 1 (e.g. Barchi *et al.* 1998; Lavecchia *et al.* 1994; Cavinato & De Celles 1999). Using both geological and seismological evidences, several authors (Aringoli *et al.* 2016; EMERGEO 2016; Falcucci *et al.* 2016; Pucci *et al.* 2017) identified the fault with several different segments of the Laga Mounts fault system (Campotosto and Amatrice fault segments, in Fig. 1, CF and AFs, respectively). Seismic activity continued for the next months, aftershocks being concentrated in a roughly 50-km-long area extending towards Norcia. It culminated with an M_w 5.9 earthquake, which occurred on 26 October at the northernmost extent of the sequence, and with a M_w 6.5 event, the largest of the sequence, on 30 October.

In this paper, we focus on the Amatrice earthquake, the first main event of the seismic sequence, since it caused major destruction with macroseismic intensities up to 10–11 (QUEST 2016; Zanini *et al.* 2016; Galli *et al.* 2016a,b). The rupture history inferred by

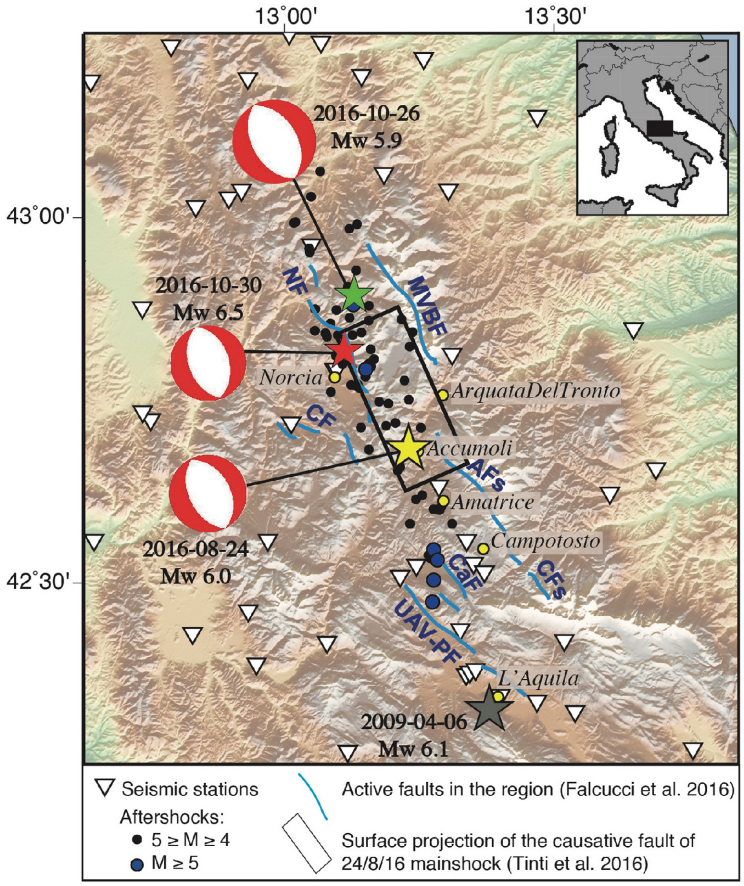

Figure 1. Map showing the regional setting of the 24 August 2016 central Italy main shock. The epicentre of 24 August 2016 *M* 6.0 main shock is indicated with a yellow star. We also show epicentres of the following earthquakes: 26 October 2016 *M* 5.9 (green star), 30 October 2016 *M* 6.5 (red star) earthquakes, and L'Aquila 6 April 2019 *M* 6.1 (grey star). Seismic events occurred during the 2016 seismic sequence with magnitude over than 5 and between 4 and 5, are plotted with black and blue dots, respectively (INGV catalogue, ISIDE 2016). Active faults in the region by Falcucci *et al.* (2016) are shown as well.

Tinti *et al.* (2016) suggested evident directivity effects, with higher ground motion parameters (PGA and PGV) at stations along the rupture direction (towards N–NW) and updip towards Amatrice. Lower ground motion parameters were found at stations in the NE and SW sectors. Evident forward directivity caused by the fast rupture propagation towards NW direction along the seismogenic fault, has also been recognized through the analysis of the instrumental data (Calderoni *et al.* 2017; Lanzano *et al.* 2016; Pischiutta *et al.* 2016; Luzi *et al.* 2017; Ren *et al.* 2017).

In this study, we produced broad-band time histories for the M_w 6.0 main shock occurred on 24 August 2016. This topic is very important in modern earthquake engineering applications where the entire time-series are required. In fact, contrary to the standard practice where ground-motion intensity is evaluated through GMPEs, the entire time histories can consider the effects of amplitude, phase, frequency content and duration, particularly for large-magnitude earthquakes at closer distances.

Since the pioneering works of Hartzell (1978) and Irikura (1986), many methodologies have been proposed in last three decades for simulating realistic ground motions, spanning from deterministic physics-based models to stochastic and hybrid methods. Deterministic methods widely used for engineering purposes, are reliable at frequencies up to 0.5–1 Hz (Douglas & Aochi 2008; Pitarka *et al.* 2019), but lack the accurate representation of wave propagation at higher frequencies. In stochastic methods, heterogeneous finite source models are stochastically generated (Guatteri *et al.* 2003, 2004; Schmedes & Archuleta 2008; Schmedes *et al.* 2010), through dynamic simulations (Song *et al.* 2014) or through the statistics of inverted kinematic source models (e.g. Mai & Beroza 2003). Stochastic simulations are generally simpler and quicker and more convenient to operate, leading to determine wave propagation at higher frequencies.

In the hybrid method, adopted in this work, synthetic time-series of ground motion cover the entire frequency band of engineering interest (0–10 Hz). This method takes advantage of the strengths of a deterministic approach at low frequencies and a stochastic approach at high frequencies (e.g. Berge *et al.* 1998; Hartzell *et al.* 1999; Mai & Beroza 2003; Hartzell *et al.* 2005; Liu *et al.* 2006; Graves & Pitarka 2010; Mai *et al.* 2010; Mena *et al.* 2012). Recently, Pitarka *et al.* (2017) proposed a new rupture generator that combines deterministic (Irikura's rupture model, Irikura & Miyake 2011) and stochastic features (Graves & Pitarka 2010) designed to be used in hybrid simulation methods. Similarly, in our procedures the high-frequency seismograms (HF) are generated using a stochastic finite-fault model approach based on a dynamic corner frequency (Motazedian & Atkinson 2005; Boore 2009) while, the low-frequency seismograms (LF) were produced through forward simulations of rupture models inferred by Tinti *et al.* (2016), up to 0.5 Hz.

Simulated hybrid ground motions are validated through the comparison with data recorded at 133 strong motion stations within a distance of 150 km. We also compared our simulated ground motion parameters in terms of the PGA, PGV and SAs (0.3, 1 and 2 s) by those

estimated from two selected GMPEs to test our simulations performance against the commonly used empirical predictions. In this study, we intent to demonstrate that the region-specific parameters can be successfully used in ground motion estimations also for areas or at sites where no strong motion recordings and stations are available. The large number of recorded seismograms from the Amatrice earthquake gives us the possibility of calibrating region-specific parameters and testing and validating our simulations.

In this aim the azimuthal variability of simulated ground motion is also assessed to investigate the capability of the method of reproducing the observed directivity effect. Finally, we implemented different site amplification curves and models in order to better account for site effects.

2 GROUND MOTION DATA

The first main shock of the central Italy seismic sequence was recorded on 24 August 2016 by 350 seismic stations belonging to the Italian Strong-Motion Network managed by the Department of Civil Protection (RAN), to the Italian Seismic Network (Rete Sismica Nazionale, RSN) managed by the Istituto Nazionale di Geofisica e Vulcanologia (INGV), and to other local networks. In this study, we have used data recorded by 100 accelerometric strong-ground-motion stations of RAN network and equipped with Kinemetrics Episensor (FBA-3200 Hz) and with ETNA 18 bits or K2-Makalu 24 bits digitizers. We have also included 32 stations of RSN and 1 station of another network (Mediterranean Very Broadband Seismographic Network, MedNet). The processed data were downloaded from the ITACA database (ITalian ACcelerometric Archive, http://itaca.mi.ingv.it/ItacaNet_30/#/home). The soil site category according to the Italian seismic design code (NTC18 2018) was assigned at 42 stations through *in situ* velocity measurements and prospecting, and consequently by using the Vs_{30} parameter. These stations mainly belong to RAN network. For the remaining stations 91 (identified with symbol $*$ in Table 1), the soil site category was inferred on the basis of the outcropping lithology and other geological inferences, as published in the ITACA database.

Further details can be found in Table 1 where for each station the soil site classification is reported together with the Joyner–Boore distances with respect to fault plane, the maximum horizontal peak ground acceleration (PGA) and peak ground velocity (PGV) values recorded during the main shock. Station location is shown in Fig. 1, with the fault projection and the hypocentre of the main shock, as well as in Fig. 2. Symbol colour indicates at each station the soil site category.

3 HYBRID BROAD-BAND SIMULATION METHOD

We generated broad-band synthetic time histories following a hybrid approach using both the location of the considered 133 recording stations and the location of 961 virtual stations distributed in each 4-km grid space. The LF portion of the synthetics at all stations was calculated by using the rupture model inferred from Tinti *et al.* (2016). This model has been retrieved by using a non-negative, least squares inversion method with simultaneous smoothing and damping (Dreger *et al.* 2005) and by inverting 21 recorded strong motion waveforms belonging to both the RAN and RSN networks at frequencies up to 0.5 Hz. To generate the LF synthetic waveforms in velocity we use the forward modelling of Tinti *et al.* (2016) applied at all the stations for frequencies up to 1 Hz.

Conversely, the HF portion of synthetics was attained by using a stochastic finite-fault simulation model, based on dynamic corner frequency deeply explained in the following section (Motazedian & Atkinson 2005; Boore 2009). The broad-band time histories were then estimated merging the HF and LF ground motions in the frequency domain at each station following Mai & Beroza (2003). First, HF and LF signals were synchronized using a long- and short-time average (LTA/STA) automatic picking algorithm. To avoid mismatch in the plateau levels between the HF and LF spectrum, we rotated the two horizontal low frequency components by increments of 1°. As a criterion for the merging procedure we considered the consistency of the plateau level of acceleration in the Fourier space around the 1 Hz frequency. The application of this procedure resulted in hybrid broad-band signals related to the horizontal components of ground motion. More details can be found in Akinci *et al.* (2017).

3.1 Stochastic simulation method and parameters

The HF portion of synthetics was attained by using a stochastic finite-fault simulation model, based on dynamic corner frequency. Stochastic simulation method considers the physics-based rupture process and requires well-defined source and slip distribution, as well as path, and site effects within the region of interest. The total spectrum of ground motion at a site is given by the product of the contribution of source, path and site effects, as:

$$\mathrm{A}(\mathrm{M}_0, \mathrm{r}, \mathrm{f}) = \mathrm{E}(\mathrm{M}_0, f) \cdot \mathrm{P}(R, f) \cdot \mathrm{G}(f), \quad (1)$$

where M_0, f and R are the seismic moment, the corner frequency and the hypocentral distance from the observation point, respectively. The term $E(M_0, f)$ is related to the contribution of the seismic source while the terms $P(R,f)$ and $G(f)$ refer to the spectrum modification caused by propagation and site effects, respectively. Further description will be given in the following sections. The time-domain stochastic simulations were iteratively repeated five times following Boore (2005), who reported that the uncertainties in peak ground motions are lower than 10 per cent when the number of iterations is increased from 10 to 640 (fig. 12 in Boore 2005). Results are therefore represented by the root mean square of the five iterations at each site.

In order to generate reliable results, it is crucial to set the simulations with well-resolved model parameters since a high variability in parameters results in very different expected ground motion levels. Thus, it is important to use as much as possible *a priori* information and consolidated models. Therefore, to reproduce the high frequency part of time histories we used the regional attenuation model realized after L'Aquila earthquake (Malagnini *et al.* 2011) and the source model published soon after Amatrice earthquake (Tinti *et al.* 2016). Finally, to consider the effect of the surface velocity variations, we used the site classification given in ITACA database for each station, using three distinct curves related to sites A, B, C and D, as prescribed by the Italian seismic design code (NTC18).

3.1.1 *Finite-fault source model*

Concerning the source, we considered the kinematic source model provided by Tinti *et al.* (2016) obtained by inverting strong-motion data recorded at 21 stations. These authors used interferometric images to discriminate the fault plane among those suggested by the moment tensor solution (TDMT) released by

Table 1. Information on stations recording the 24 August 2016 central Italy main shock and considered in this study. Asterisks in the Site class column, indicate cases where the site classification according to EC-18 and NTC18 has been deduced on the basis of the local geological conditions.

Station code	Station name	NET	LAT	LON	Site class (EC18)	Mod Azimuth (deg from N)	Sector	R_{JB} dist (km)	rec PGA E-W (cm ss^{-1})	rec PGA N-S (cm ss^{-1})	rec PGV E-W (cm s^{-1})	rec PGV N-S (cm s^{-1})	Hybrid BB PGA (cm ss^{-1})	Hybrid BB PGV (cm s^{-1})	Hybrid BB PSA 0.3 s (cm ss^{-1})	Hybrid BB PSA 1 s (cm ss^{-1})	Hybrid BB PSA 2 s (cm ss^{-1})
AMT	Amatrice	IT	42.6325	13.2866	**B**	172	S	0.88	850.80	368.39	43.55	41.50	599.74	29.25	0.940	0.193	0.046
ANB	Ancona2	IT	43.5922	13.5074	**B***	37	N	83.06	30.75	23.69	2.10	1.90	14.32	1.73	0.026	0.025	0.005
ANT	Antrodoco	IT	42.4182	13.0786	**A**	226	S	26.16	14.09	23.08	2.42	3.82	53.56	2.75	0.115	0.049	0.007
APEC	Apecchio	IV	43.55846	12.41991	**B***	350	N	97.18	1.34	1.46	0.22	0.29	5.64	0.71	0.022	0.012	0.002
AQF	LAquila Fiume Aterno	IT	42.3807	13.3547	**B***	188	S	28.77	43.38	37.25	2.62	2.40	52.93	4.53	0.111	0.043	0.017
AQG	L'Aquila—Colle Grilli	IT	42.3737	13.337	**B**	190	S	29.05	50.95	58.01	5.01	5.17	53.85	3.23	0.170	0.046	0.015
AQK	LAquila Aquilpark	IT	42.345	13.4009	**B**	184	S	33.86	49.52	57.03	9.03	9.80	45.18	4.60	0.142	0.059	0.014
AQU	Aquila Castello	MN	42.3539	13.4019	**B***	184	S	32.99	23.08	25.34	3.25	4.29	46.00	3.13	0.110	0.032	0.010
AQV	LAquila Centro Valle	IT	42.3771	13.3439	**B**	189	S	28.86	59.60	45.27	3.93	4.40	55.73	4.76	0.174	0.053	0.014
ASP	Ascoli Piceno	IT	42.848	13.6479	**B**	88	N	31.36	86.76	85.72	3.45	3.12	73.58	6.20	0.130	0.078	0.016
ASS	Assisi	IT	43.075	12.6041	**B***	333	N	48.24	42.11	21.57	1.87	1.88	34.99	2.26	0.110	0.049	0.009
ATCC	Casa Castalda	IV	43.18514	12.63994	**B***	342	N	53.67	28.37	22.60	1.81	2.19	25.28	2.18	0.072	0.030	0.008
ATFO	Monte Foce—Gubbio	IV	43.3666	12.5715	**B***	348	N	72.65	9.56	11.57	1.33	1.41	14.79	1.37	0.034	0.016	0.006
ATLO	Monte Lovesco	IV	43.31516	12.40726	**B***	339	N	77.38	5.87	6.80	1.07	1.20	16.44	1.98	0.043	0.026	0.010
ATN	Atina	IT	41.6203	13.8012	**A***	182	S	120.75	2.24	3.16	0.58	0.73	3.86	0.63	0.009	0.013	0.004
ATPC	Poggio Castellaccio	IV	43.4807	12.457	**B***	348	N	88.40	11.21	7.75	1.24	1.65	12.76	1.11	0.029	0.024	0.008
ATTE	AVT—Monte Tezio	IV	43.1979	12.3536	**A***	332	N	72.84	4.70	4.92	0.81	0.93	7.24	1.06	0.019	0.013	0.002
ATVO	AVT—Monte Valentino	IV	43.38211	12.40663	**B***	342	N	82.65	6.11	5.53	0.97	1.23	11.29	1.25	0.038	0.022	0.003
AVZ	Avezzano	IT	42.0274	13.4259	**C**	192	S	68.11	9.79	13.32	1.61	1.92	23.81	2.58	0.048	0.039	0.013
BSS	Bussi	IT	42.1917	13.8453	**B***	162	S	66.26	14.07	20.97	1.25	2.37	17.21	1.89	0.039	0.025	0.007
BTT2	Borgo Ottomila 2	IT	41.99833	13.54306	**D**	186	S	73.89	22.01	24.94	6.68	8.49	35.54	3.45	0.094	0.064	0.016
BVG	Bevagna	IT	42.9323	12.611	**C**	321	N	41.37	39.14	49.22	5.97	6.22	48.97	3.75	0.138	0.038	0.017
BZZ	LAquila Bazzano	IT	42.337	13.4685	**B**	178	S	36.92	24.73	28.88	2.84	3.49	46.62	2.99	0.104	0.032	0.009
CADA	Capodarco	IV	43.1942	13.7614	**B***	62	N	57.17	30.45	33.97	5.72	5.65	28.78	2.21	0.059	0.029	0.016
CCT	Città di Castello	IT	43.3683	12.2346	**C**	337	N	91.90	17.05	19.12	2.72	1.85	10.49	1.55	0.020	0.020	0.010
CDCA	Città di Castello	IV	43.4584	12.2336	**C**	340	N	98.63	7.45	11.90	1.22	2.82	13.29	2.09	0.031	0.035	0.012
CERA	Filignano	IV	41.5978	14.0183	**A***	176	S	130.23	2.62	2.64	0.71	0.62	3.18	0.37	0.009	0.005	0.002
CIMA	Cittanova Marche	IV	43.3053	13.67009	**B**	52	N	60.61	21.75	18.11	4.75	3.48	17.59	1.89	0.049	0.022	0.007
CLF	Colfiorito	IT	43.03671	12.92043	**D**	350	N	26.09	122.98	128.78	8.70	11.64	142.94	15.43	0.380	0.329	0.059
CLN	Celano	IT	42.0852	13.5207	**B***	185	S	64.27	7.42	4.22	0.55	0.77	14.08	1.26	0.041	0.021	0.005
COR1	Corinaldo	IV	43.63183	13.00033	**B***	14	N	85.56	21.68	16.29	2.96	3.05	11.89	1.65	0.031	0.019	0.005
CPS	Capestrano	IT	42.2716	13.7583	**B**	161	S	54.89	11.50	11.45	0.97	1.22	23.52	2.11	0.051	0.022	0.008
CSA	Castenuovo Assisi	IT	43.008	12.5906	**C**	327	N	45.69	41.78	47.83	8.06	10.91	52.26	5.94	0.112	0.093	0.029
CSC	Cascia	IT	42.7191	13.01228	**B**	301	N	12.28	104.78	82.03	6.15	7.72	174.79	10.29	0.365	0.087	0.037
CSD	Castel Viscardo	IT	42.754	12.0035	**B**	298	N	90.31	6.55	7.72	1.27	0.99	9.99	1.50	0.019	0.029	0.003
CSO1	Carsoli 1	IT	42.1009	13.088	**B***	214	S	59.33	11.41	7.28	1.47	1.15	18.72	2.07	0.050	0.032	0.006
CSS	Cassino	IT	41.4858	13.8231	**B**	184	S	135.29	1.94	1.91	0.46	0.31	4.34	0.49	0.010	0.013	0.003
CTD	Cittaducale	IT	42.3884	12.9477	**B**	238	S	35.12	31.39	23.22	2.07	1.99	36.79	3.70	0.092	0.032	0.011
CTL	Cattolica	IT	43.955	12.7358	**C**	8	N	125.84	16.62	16.69	2.24	2.41	9.16	1.10	0.016	0.021	0.008
CTS	Citta di Castello	IT	43.4919	12.2233	**C***	341	N	101.84	10.96	11.53	2.04	3.54	17.26	2.23	0.029	0.055	0.007
FBR	Fabriano	IT	43.3436	12.9119	**C***	4	N	57.24	46.70	37.96	2.50	2.29	47.01	3.30	0.079	0.048	0.017
FEMA	Monte Fema	IV	42.9621	13.04976	**B***	357	N	13.94	242.34	185.82	14.56	9.17	119.50	9.38	0.231	0.051	0.021
FIU1	Fiuminata	IV	43.18856	12.9316	**B***	0	N	40.85	28.24	38.40	1.58	1.69	27.68	2.77	0.123	0.025	0.010
FLT	Filettino	IT	41.8933	13.3254	**B***	199	S	81.52	3.87	3.76	0.69	0.64	10.00	1.27	0.021	0.018	0.007
FMG	Fiamignano	IT	42.268	13.1172	**B**	215	S	40.69	16.91	15.88	1.92	1.99	31.33	2.47	0.062	0.031	0.009
FOC	Foligno Colfiorito	IT	43.0263	12.8965	**C***	347	N	26.50	256.20	322.54	8.10	10.18	61.78	4.39	0.140	0.057	0.018

Table 1. Continued

Station code	Station name	NET	LAT	LON	Site class (EC18)	Mod Azimuth (deg from N)	Sector	R_{JB} dist (km)	rec PGA E-W (cm ss^{-1})	rec PGA N-S (cm ss^{-1})	rec PGV E-W (cm s^{-1})	rec PGV N-S (cm s^{-1})	Hybrid BB PGA (cm ss^{-1})	Hybrid BB PGV (cm s^{-1})	Hybrid BB PSA 0.3 s (cm ss^{-1})	Hybrid BB PSA 1 s (cm ss^{-1})	Hybrid BB PSA 2 s (cm ss^{-1})
FOS	Foligno Seggio	IT	43.0146	12.8351	**B***	341	N	29.06	58.70	74.99	5.26	4.83	56.31	3.53	0.100	0.052	0.011
FOSV	Fossato di Vico	IV	43.29483	12.76117	**B***	12	N	57.51	22.54	27.84	1.21	2.23	19.77	1.97	0.075	0.034	0.010
FRT	Ferentino	IT	41.6926	13.255	**B***	203	S	103.49	3.38	4.83	0.79	0.79	7.07	1.01	0.021	0.017	0.005
FSS	Fossombrone Marche	IT	43.6905	12.8101	**C***	7	N	96.07	7.30	6.17	0.57	0.91	11.58	1.27	0.023	0.027	0.005
GAG1	Gagliolo	IV	43.23806	13.06743	**B***	12	N	41.74	75.89	89.47	6.48	7.27	34.32	2.56	0.086	0.030	0.008
GBB	Gubbio	IT	43.3569	12.5972	**B***	349	N	70.54	18.50	14.68	1.30	1.58	15.62	1.71	0.032	0.047	0.004
GBC	Gubbio	IT	43.3553	12.5726	**C***	348	N	71.59	11.34	9.15	1.24	1.70	19.79	2.91	0.034	0.047	0.017
GBP	Gubbio Piana	IT	43.3138	12.5894	**C**	347	N	67.11	29.27	34.77	9.25	6.15	23.86	3.01	0.041	0.056	0.015
GLT	Gualdo Tadino	IT	43.2331	12.789	**C***	353	N	50.43	21.01	15.28	1.54	1.83	32.67	2.67	0.075	0.047	0.013
GNU	Giano nellUmbria	IT	42.8038	12.5702	**A***	306	N	43.68	21.24	23.91	1.49	2.03	17.71	1.96	0.044	0.013	0.005
GRD	Guardiagrele	IT	42.1785	14.1798	**A***	150	S	86.83	2.28	1.67	0.33	0.30	6.55	0.97	0.015	0.012	0.004
GRN	Guarcino	IT	41.8134	13.3169	**A***	200	S	90.31	3.44	3.51	0.69	0.87	5.98	0.82	0.014	0.013	0.005
GSA	Assergi Gran Sasso	IT	42.4207	13.5194	**B**	166	S	30.22	35.40	36.42	1.90	2.56	58.61	3.16	0.108	0.072	0.012
LDP	Lama dei Peligni	IT	42.03917	14.18263	**C**	156	S	97.28	6.56	6.36	0.71	0.98	9.91	1.59	0.023	0.027	0.010
LSS	Leonessa	IT	42.5582	12.9689	**A**	258	S	22.78	23.04	18.99	2.05	2.28	61.78	4.18	0.179	0.074	0.011
MCR	Macerata Feltria	IT	43.7998	12.4475	**C***	357	N	119.10	10.91	9.23	0.89	1.27	7.81	1.44	0.017	0.019	0.007
MCT	Macerata	IT	43.2925	13.4189	**B***	37	N	49.18	75.03	80.46	7.75	6.94	32.47	4.37	0.093	0.043	0.013
MDAR	Monte Daria	IV	43.1927	13.1427	**B***	17	N	35.47	38.94	54.61	3.44	3.71	32.21	2.55	0.107	0.036	0.007
MGAB	Monte Gabbione	IV	42.91263	12.11214	**A***	308	N	81.28	8.96	9.61	1.19	1.17	8.76	1.21	0.020	0.014	0.005
MMP1	Mompeo	IT	42.2492	12.7483	**A**	243	S	57.53	8.40	11.50	0.82	1.32	11.02	0.99	0.036	0.021	0.006
MMUR	Monte Murano	IV	43.44183	12.9973	**A***	11	N	65.08	20.59	22.24	1.82	2.46	10.21	1.37	0.021	0.011	0.005
MNF	MonteFiegni Fiastra	IT	43.0596	13.1844	**A***	19	N	20.36	71.66	43.46	4.77	2.90	55.82	3.65	0.104	0.067	0.010
MNTP	Montappone	IV	43.13738	13.46925	**B***	46	N	35.83	79.11	72.41	6.17	5.09	40.10	4.72	0.112	0.070	0.013
MSC	Mascioni Campotosto	IT	42.5268	13.3508	**B**	177	S	13.74	103.54	75.59	7.72	5.62	197.06	11.36	0.462	0.184	0.022
MSCT	Mascioni Campotosto 2	IT	42.5267	13.3509	**B***	177	S	13.76	107.99	77.52	7.97	5.74	133.89	12.32	0.313	0.149	0.035
MTL	Matelica	IT	43.2494	13.0083	**B**	8	N	44.51	69.95	66.71	3.72	6.47	26.12	2.57	0.074	0.041	0.008
MTR	Montereale	IT	42.524	13.2447	**A***	200	S	11.14	79.13	75.44	11.45	8.67	89.26	6.87	0.190	0.079	0.022
MURB	Monte Urbino	IV	43.263	12.5246	**B***	342	N	66.45	45.60	40.57	3.11	3.28	22.61	2.22	0.039	0.031	0.011
MVB	Monte Vibiano	IT	42.9619	12.257	**A**	314	N	70.34	4.85	5.63	0.83	0.89	9.80	0.96	0.032	0.012	0.005
NOR	Norcia La Castellina	IT	42.7924	13.0924	**B**	336	N	2.98	197.91	176.67	27.13	21.10	441.75	27.12	0.781	0.317	0.087
NRC	Norcia	IT	42.7925	13.0964	**B**	337	N	2.67	352.87	366.77	29.75	23.70	307.66	19.03	0.506	0.164	0.104
NRN	Narni	IT	42.5155	12.5194	**A***	275	N	58.26	8.54	7.75	1.07	0.92	15.56	1.78	0.036	0.022	0.005
OCAN	Cantiano	IT	43.4723	12.6308	**B***	355	N	79.92	11.72	11.61	0.81	0.83	16.06	2.11	0.039	0.040	0.009
PAN	Panicale	IT	43.0058	12.1436	**B***	315	N	80.42	5.06	3.98	0.58	0.79	17.64	1.91	0.027	0.035	0.006
PCB	Poggio Cancelli	IT	42.558	13.338	**B***	175	S	10.15	185.15	301.85	8.14	13.08	232.67	11.72	0.318	0.225	0.026
PGG	Poggio Picenze	IT	42.3229	13.5394	**B***	173	S	40.70	44.71	44.78	2.51	2.17	45.25	3.13	0.096	0.044	0.007
PIEI	Pieia	IV	43.53567	12.535	**A***	353	N	89.93	8.33	6.11	0.67	0.70	6.18	0.72	0.013	0.007	0.003
PNC	Piancastagnaio	IT	42.8474	11.6935	**B***	302	N	115.11	3.67	2.58	0.85	0.70	7.29	1.27	0.021	0.015	0.006
PNN	Pennabilli	IT	43.8181	12.2628	**C**	352	N	128.31	8.74	8.48	2.32	1.95	9.13	1.00	0.020	0.015	0.007
POFI	Posta Fibreno	IV	41.71743	13.71202	**A***	184	S	108.02	2.55	2.29	0.60	0.47	4.07	0.50	0.010	0.007	0.002
PP3	Marolino	IV	43.37783	13.6095	**C***	46	N	64.48	49.58	40.43	4.17	2.90	26.93	3.21	0.053	0.031	0.009
PSC	Pescasseroli	IT	41.812	13.7892	**A**	179	S	100.86	3.21	4.46	0.92	0.83	4.79	0.60	0.015	0.008	0.004
PTI	Petritoli	IT	43.0665	13.657	**B***	64	N	42.14	37.83	36.80	3.89	3.77	32.60	3.52	0.088	0.025	0.015
PTL	Pietralunga	IT	43.4273	12.4485	**B***	346	N	84.15	11.12	12.49	1.31	1.80	8.16	0.92	0.029	0.015	0.003
PZI1	Pizzoli	IT	42.4356	13.3262	**B***	189	S	22.24	44.34	45.15	4.34	4.71	71.24	5.89	0.189	0.106	0.012
RM33	Pellescritta	IV	42.50898	13.21452	**B***	207	S	12.88	100.36	99.03	9.30	6.25	118.33	5.87	0.279	0.051	0.022
RNI2	Rionero Sannitico	IV	41.70328	14.1524	**A***	169	S	125.16	4.64	4.54	0.99	1.36	2.87	0.45	0.006	0.008	0.003
ROM9	Roma (sede INGV)	IV	41.82842	12.51553	**B**	236	S	106.11	4.60	3.37	0.87	0.81	11.12	0.92	0.020	0.013	0.003

Table 1. Continued

Station code	Station name	NET	LAT	LON	Site class (EC18)	Mod Azimuth (deg from N)	Sector	R_{JB} dist (km)	rec PGA E-W (cm ss^{-1})	rec PGA N-S (cm ss^{-1})	rec PGV E-W (cm s^{-1})	rec PGV N-S (cm s^{-1})	Hybrid BB PGA (cm ss^{-1})	Hybrid BB PGV (cm s^{-1})	Hybrid BB PSA 0.3 s (cm ss^{-1})	Hybrid BB PSA 1 s (cm ss^{-1})	Hybrid BB PSA 2 s (cm ss^{-1})
RQT	Arquata del Tronto	IT	42.813	13.311	**A**	52	N	4.63	447.87		13.85		260.70	12.24	0.564	0.172	0.050
RTI	Rieti	IT	4243020	1282900	**D**	252	S	38.53	29.25	27.63	4.12	4.34	86.01	6.68	0.159	0.097	0.025
SACS	San Casciano dei Bagni	IV	42.84906	11.90967	**B***	303	N	97.45	4.16	4.14	1.15	1.25	8.07	1.15	0.019	0.019	0.004
SBC	Subiaco	IT	41.9132	13.1055	**A**	211	S	79.66	3.43	5.76	0.92	0.84	9.20	1.02	0.025	0.015	0.007
SBT	S. Benedetto	IT	42.9338	13.8604	**B***	87	N	51.10	37.46	29.15	2.54	3.18	27.70	3.03	0.074	0.040	0.013
SCF	Scafa	IT	42.2651	13.9985	**B***	151	S	69.25	28.99	33.17	2.22	2.17	9.39	1.29	0.033	0.018	0.005
SENI	Senigallia	IV	43.7052	13.2331	**C**	24	N	92.00	42.92	26.48	2.41	2.79	17.92	2.47	0.034	0.034	0.008
SIG	Sigillo	IT	43.3308	12.7408	**C***	355	N	61.82	20.58	24.93	0.99	1.85	28.68	3.14	0.051	0.032	0.010
SNG	Senigallia	IT	43.6855	13.2261	**C**	24	N	89.80	38.16	45.12	3.40	3.54	17.61	2.21	0.047	0.033	0.006
SNI	Sangemini	IT	42.632	12.554	**B***	286	N	50.41	32.73	29.77	2.69	2.82	28.37	1.98	0.063	0.035	0.006
SNO	Sarnano	IT	43.03717	13.30414	**B***	33	N	19.35	90.31	47.14	4.78	4.24	163.60	10.12	0.322	0.098	0.027
SNS1	Sansepolcro	IT	43.5735	12.1312	**C***	342	N	113.58	11.28	11.10	2.60	2.15	8.40	1.50	0.017	0.033	0.008
SOR	Sora	IT	41.7203	13.6136	**B***	188	S	105.07	6.86	5.74	0.93	0.96	8.53	1.33	0.015	0.021	0.006
SPD	Sella Pedicate	IT	42.5151	13.371	**B***	175	S	15.60	51.91	99.85	4.98	7.63	163.41	8.76	0.299	0.148	0.034
SPM	Spoleto Monteluco	IT	42.7232	12.7512	**A***	298	N	31.57	65.95	63.55	2.39	3.04	39.45	3.21	0.078	0.048	0.013
SPO1	Spoleto 2	IT	42.7344	12.7363	**B***	300	N	32.20	47.84	44.81	3.60	4.43	66.25	3.97	0.136	0.046	0.009
SRL	Sirolo	IT	43.5179	13.6193	**C**	43	N	78.63	18.13	25.74	0.96	1.54	17.72	2.46	0.043	0.034	0.016
SSFR	Montelago Sassoferrato	IV	43.43628	12.78225	**A***	0	N	70.95	57.11	49.55	2.44	1.84	7.70	0.69	0.019	0.017	0.002
SSG	Sansepolcro Citta	IT	43.5698	12.1463	**B***	342	N	112.42	9.19	8.18	1.71	2.38	5.58	0.77	0.015	0.012	0.004
SSO	Sansepolcro Ospedale	IT	43.5715	12.154	**B***	342	N	112.12	4.56	5.94	1.27	2.17	7.01	0.89	0.012	0.011	0.004
SUL	Sulmona	IT	42.0895	13.9343	**A***	163	S	79.68	5.79	6.07	0.88	0.79	6.49	1.05	0.015	0.011	0.006
SULA	Sulmona autoparco	IT	42.0734	13.9166	**C***	165	S	80.26	18.03	23.23	3.74	3.83	15.63	1.88	0.038	0.033	0.008
SULC	Sulmona consorzio	IT	42.068	13.909	**C***	165	S	80.39	13.41	15.70	1.99	2.54	21.45	1.98	0.048	0.046	0.009
SULP	Sulmona polizia	IT	42.085	13.9274	**B***	164	S	79.74	22.18	22.10	2.70	2.97	10.46	1.15	0.032	0.026	0.008
TER	Terelle	IT	42.6565	13.6895	**A***	121	S	28.40	64.78	41.36	4.00	2.79	45.46	3.73	0.083	0.059	0.012
TERO	Teramo	IV	42.62279	13.60393	**B***	130	S	21.78	55.54	83.55	3.16	4.30	123.07	8.57	0.262	0.124	0.030
TLN	Tolentino	IT	43.2159	13.2584	**B**	26	N	37.83	116.17	74.76	7.10	5.90	39.38	3.20	0.074	0.051	0.016
TOD	Todi	IT	42.7381	12.3873	**A***	298	N	59.55	18.73	12.94	2.37	1.93	15.33	1.75	0.052	0.021	0.006
TRE	Trevi	IT	42.8765	12.7358	**C***	320	N	30.19	62.96	108.50	6.11	7.81	49.18	5.14	0.157	0.078	0.021
TRE1	Treia	IV	43.3112	13.31285	**B***	30	N	48.93	62.08	71.31	6.08	4.35	34.74	3.44	0.053	0.035	0.008
TRL	Terminillo	IT	42.4613	12.9323	**B**	247	S	30.58	34.88	38.43	3.96	3.74	45.16	4.88	0.153	0.042	0.020
TRN1	Terni 2	IT	4255820	1264610	**D***	276	S	45.91	9.17	13.64	1.00	1.08	55.96	5.63	0.164	0.080	0.021
TSC	Tuscania	IT	42.4226	11.8696	**A***	279	N	110.96	7.11	3.76	1.14	1.07	5.50	0.66	0.012	0.009	0.004
TVL	Tivoli	IT	41.893	12.7732	**B***	227	S	89.52	14.22	16.27	1.87	1.71	8.87	1.16	0.019	0.014	0.004
UMB	Umbertide	IT	43.2544	12.2556	**B***	332	N	82.97	8.39	8.84	1.16	0.98	12.10	1.58	0.038	0.025	0.006
VAL	Valfabbrica	IT	43.1593	12.6017	**B***	339	N	54.00	58.27	35.82	1.95	1.84	35.58	3.21	0.055	0.059	0.010
VLL	Velletri	IT	41.6704	12.7726	**B***	222	S	112.45	5.20	6.34	1.68	1.25	5.22	0.76	0.012	0.009	0.005
VLN	Valiano	IT	43.1427	11.8947	**C***	319	N	104.17	10.16	10.80	2.14	2.54	10.25	1.42	0.034	0.015	0.009
VSE	Vasto	IT	42.1221	14.7071	**B***	141	S	126.50	6.12	6.10	1.15	0.90	5.36	0.72	0.013	0.011	0.003

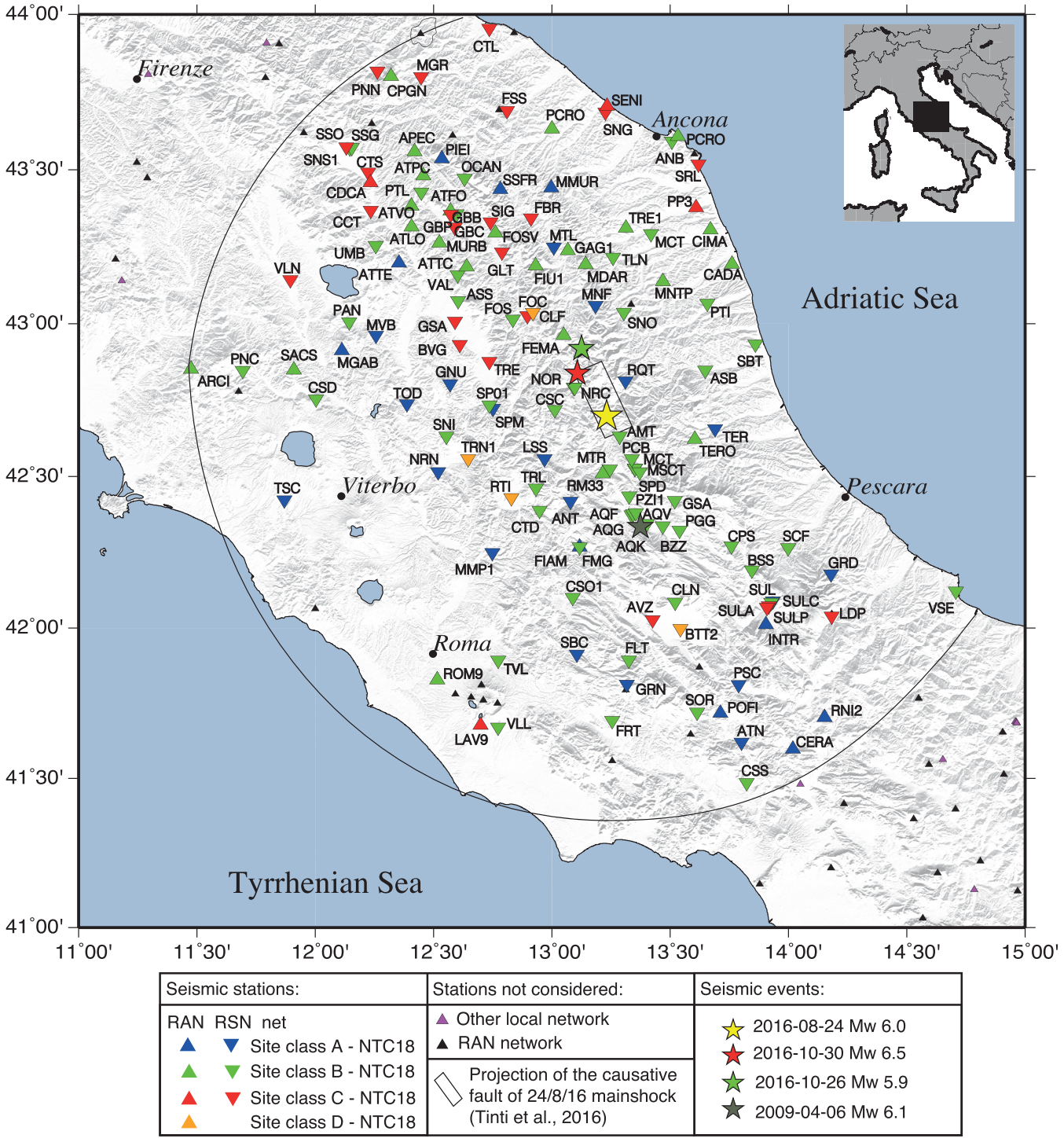

Figure 2. Map showing stations considered in this study, belonging to RAN network and up to an epicentral distance of 150 km (reverse triangles). We also included some stations of RSN network (triangles). Symbol colour is related to site classification according to NTC18 on the basis of Vs_{30} parameter We also plot stations belonging to other networks (RSN and local) that we have not considered.

INGV (http://cnt.rm.ingv.it/event/7073641/?tab=MeccanismoFocale-TDMTinfo), finally proposing a fault plane with N156° strike and 50° dip (towards SW). The adopted fault dimension is 26 km long and 16 km width. The Green's functions are computed by using the CIA (Central Italian Apennines) 1-D velocity model inferred for the Central Apennines during the 2009 L'Aquila sequence (Herrmann *et al.* 2011).

This multiwindow rupture model is composed by three-time windows not overlapped in time and activated with relatively fast rupture velocity (3.1 km s^{-1}) and a constant rise time of 1.2 s (for each time window). The total inferred seismic moment is 1.6 × 1018 Nm, corresponding to a magnitude M_w of 6.1. The rupture is bilateral and the inferred slip distribution shows two main slip patches: the southeastern one (4 km updip from the hypocentre) has a relatively

large maximum slip (99 cm), with a rake roughly around 120° while the northwestern patch is the largest one and is located ∼10 km from the hypocentre at a similar depth ∼4.2 km, with an average mean slip of 55 cm and rake roughly 70°.

The slip distribution proposed by Tinti *et al.* (2016, Fig. 3) was used in our stochastic simulation, interpolating the fault surface from the original 2 km × 2 km subfaults into 0.5 km × 0.5 km subfaults, and using a k^2 fault slip spectrum (Herrero & Bernard 1994).

Motazedian & Atkinson (2005) proposed an implementation of Boore (2009) method, based on a dynamic corner frequency approach. Since the slipping portion of the fault increases with time, also the corner frequency of the subfaults would decrease with time, decreasing radiated energy at high frequencies. Thus, the percentage of pulsing area controls the level of spectra at low frequencies. Ground motion of the entire fault is estimated by summing up the contributions of each subfault and using a relative delay time Δt_{ij} the wave radiated from the *ij*th subfault to reach the observation point, where *nl* and *nw* are the number of subfaults along the length and width of the main fault:

$$\mathrm{a}\,(\mathrm{t}) = \sum_{i=1}^{nl}\sum_{j=1}^{nw} a_{ij}\left(t + \Delta t_{ij}\right) \tag{2}$$

The contribution of the *ij*th subfault on the acceleration spectrum is expressed as:

$$E_{ij}\left(\mathrm{M}_{0ij}, \mathrm{f}\right) = \left\{\mathrm{CM}_{0ij} Hij (2\pi \mathrm{f})^2 / \left[1 + \left(\mathrm{f}/\mathrm{f}_{0ij}\right)^2\right]\right\}, \tag{3}$$

where M_{0ij}, f_{0ij} and R_{ij} are the *ij*th subfault seismic moment, dynamic corner frequency and distance from the observation point, respectively. The term H_{ij} is a scaling factor inserted by Motazedian & Atkinson (2005) to conserve the high-frequency spectral level of subfaults. The constant C is given by:

$$\mathrm{C} = \Re^{\theta\varphi}\, FV / \left(4\pi\rho\beta^3\right), \tag{4}$$

where $\Re$ is the radiation pattern, F is the free surface amplification (2.0), V is partition into two horizontal components (0.71), β is shear wave velocity and ρ is the density.

The dynamic corner frequency of the *ij*th subfault is defined as a function of the stress drop ($\Delta\sigma$ in bar) and seismic moment (M_0 in dyne.cm) of each *ij*th subfault following equation (Boore 2003):

$$\mathrm{f}_{0ij}\,(t) = N_R(t)^{-\frac{1}{3}}\, 4.9 \times 10^6 \beta \sqrt[3]{\left(\frac{\Delta\sigma}{\mathrm{M}_0}\right)}. \tag{5}$$

According to Ugurhan *et al.* (2010), we adopted a value of 150 bar for the stress drop, $\Delta\sigma$. This latter parameter controls the high-frequency spectral amplitudes. In order to conserve the high-frequency spectral level of the subfaults, considering the corner frequency as a function of time, Motazedian & Atkinson (2005) introduced the scaling factor $\mathrm{N_R(t)}^{-\frac{1}{3}}$ in eq. (5). Consequently, the corner frequency is dependent on the cumulative rupture area, rupture beginning at high corner frequencies and progressing to lower ones with the rupture evolution. The major advantage of the dynamic corner frequency approach is that the high-frequency energy radiated is conserved regardless of subfault size and the method can be used for a broader magnitude range. All the spectral source parameters used for the HF ground-motion simulations are listed in Table 2.

3.1.2 High-frequency seismic wave attenuation model

Seismic attenuation in stochastic simulation plays a major role, controlling the overall shape and amplitude of simulated spectra. Following eq. (1) the contribution of the path is given by the term $P(R, f)$ that is represented on average as a combination of geometrical spreading $Z(R)$ and anelastic attenuation as follow:

$$\mathrm{P}\,(R, f) = \mathrm{Z}\,(R) \cdot \exp\left(-\frac{\pi \mathrm{f R}_{ij}}{\mathrm{Q}\beta}\right). \tag{6}$$

In this study, to set the attenuation parameters, we used a well-resolved region-specific attenuation model published after the 2009 L' Aquila earthquake and proposed by Malagnini *et al.* (2011). It was obtained from several regressions of 170 weak-motion records belonging to foreshocks and aftershocks of the 2009 L'Aquila seismic sequence. This model was realized through regression analyses of velocity time-series and Fourier spectra from 0.1 to 10 Hz, recorded at distances between 40 and 350 km, by using a narrow bandpass filter evaluated on the basis of the corner frequency of the event. It provides the average features of three contributions in the wave propagation: geometrical attenuation, anelastic attenuation and ground motion duration.

The parameters adopted in this study are listed in Table 3. For distances beyond 100 km, we set for the geometrical parameter $Z(R)$ a value $r^{-0.5}$ similar to the theoretical one expected for surface waves. For shorter distance we set $r^{-1.1}$ and $r^{-1.0}$ similarly to the expected value for the body waves propagation in the crustal. The regional anelastic attenuation is represented on average as a function of frequency, as reported in Table 3.

3.1.3 Site amplification for generic soil classes

Site effects refer to contribute of local site geology on ground motion. They are very important since they can strongly affect the amplitude, frequency content, and duration of ground motion. They depend on the seismic velocity pattern and the presence of velocity and impedance contrast in the subsoil. According to Boore (2003), the frequency-dependent modification of seismic spectrum due to site effects [$G(f)$ in eq. 1] are considered in the stochastic simulation computer code, EXSIM, through the combination of the amplification [$A(f)$] and attenuation [$D(f)$] contributions as follow:

$$G\,(f) = A\,(f) \cdot D\,(f). \tag{7}$$

The term $A(f)$ refers to wave amplification, while the term $D(f)$ is a diminution operator accounting for de-amplification effects from the near-surface and given by:

$$D\,(f) = \exp\left(-\pi\kappa_0 \mathrm{f}\right). \tag{8}$$

It is defined through the κ_0 filter according to Anderson & Hough (1984). Site effects are taken into account in seismic design codes of many countries through the shear wave velocity profile and the average shear-wave velocity of the subsoil in the first 30 m, given by the Vs_{30} parameter. The Italian seismic design prescribes five classes:

$$\text{NTC - 18}\begin{cases} Vs_{30} > 800\ \mathrm{m\,s^{-1}} & \text{class-A} \\ 800\ \mathrm{m\,s^{-1}} > Vs_{30} > 360\ \mathrm{m\,s^{-1}} & \text{class-B} \\ 360\ \mathrm{m\,s^{-1}} > Vs_{30} > 180\ \mathrm{m\,s^{-1}} & \text{class-C} \\ Vs_{30} < 180\ \mathrm{m\,s^{-1}} & \text{class-D} \\ \text{particular cases} & \text{class-E} \end{cases} \tag{9}$$

For the considered 133 stations, the shear-wave velocity profile measured *in situ* is provided in ITACA database only for a minor

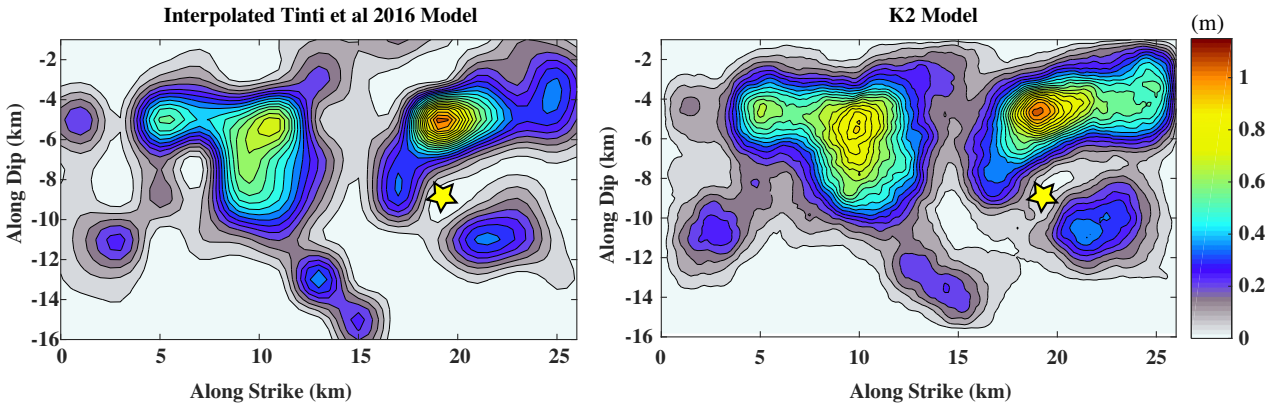

Figure 3. Slip model distribution by Tinti *et al.* (2016) adopted in this study. The yellow star indicates the hypocentre of the 24 August 2016 main shock. Left-hand panel: original slip model by Tinti *et al.* (2016); Right-hand panel: slip model obtained applying the k^2 distribution.

Table 2. Spectral source parameters used in the high frequency (HF) stochastic ground-motion simulations considering the fault slip model by Tinti *et al.* (2016).

Source parameters	
Fault orientation (strike and dip)	156°–50°
Fault dimensions (km)	26.5 × 15
Moment magnitude	6.0
Corner of the upper edge (lat, lon)	42.87726 13.21006
Depth of the top of the fault plane (km)	0.25
Subfault dimensions (km)	0.5 × 0.5
Source spectrum model	Single corner-frequency, ω^2
Stress parameter, $\Delta\sigma$ (bars)	150.0
Shear-wave velocity at source depth, β (km s^{-1})	3.2
Density at source depth, ρ (g cc^{-1})	2.8
Rupture propagation speed (km s^{-1})	fixed at 3.1 km s^{-1}
Pulsing area percentage	0.5

Table 3. Spectral propagation parameters used in the high frequency (HF) stochastic ground-motion simulations.

Propagation parameters	
Geometric spreading, $Z(r)$	$R^{-1.1}$ *for* $1 < R < 10$ km $R^{-1.0}$ *for* $10 < R < 40$ km $R^{-0.7}$ *for* $40 < R < 100$ km $R^{-0.5}$ *for* $R > 100$ km
Anelastic attenuation, $Q(f)$	$275(10f)^{-2}$ *for* $f < 0.2$ Hz $68.75(5f)^{0.584}$ *for* $0.2 < f < 0.6$ Hz $140f^{0.25}$ *for* $f > 0.6$ Hz
Kappa k_0 (s)	0.02 for A class (NTC18) 0.03 for B class (NTC18) 0.04 for C class (NTC18) 0.045 for D class (NTC18)
Other parameters	
Source duration	1/fa
Distance-dependent duration	0.05R
Windowing function	Saragoni & Hart (1974)

percentage of them (42 over 133 stations). Therefore, in the absence of direct measurements, the soil site category according to the Italian seismic design code (NTC18) was derived from indirect evaluations made considering the outcropping lithology and the inferred geological structure. In this case an asterisk is added in Table 1 after the subsoil site class. Even if the assignment of the site class on the basis of the outcropping lithology is a common practice when the velocity profile is missing, we stress that it can lead to a wrong estimate of local site response due to unpredicted effects as vertical and/or lateral variation of geotechnical properties due to the sedimentation process, heterogeneities in volcanic deposits due to palaeosoils and palaeo-topographies, presence of fractures in rocks, and many others related to geological assessment variability.

Since for the most part of stations the velocity profile was not available, in this study we needed to use amplification curves representative of the different site classes (eq. 9). Many studies in literature have provided generic amplification curves for the National Earthquake Hazard Reduction Program, NEHRP, seismic code adopted in the United States, U.S. (e.g. Boore & Joyner 1997; Boore 2003, 2016; Campbell & Boore 2016). However, the class threshold for Italian and U.S. seismic design code are different, as shown in Table 4. Such differences between seismic codes reflect the different geological context and lithological features of the two countries. As an example, while for the NTC18 the seismic bedrock is represented by the uppermost class-A with Vs_{30} over 800 m s^{-1}, in the NEHRP it involves rocks with Vs_{30} over 1500 m s^{-1}, represented by the 'Hard Rock profile' (e.g. Atkinson & Boore 2006). Another example regards the 'Generic rock profile' (Boore 2016), related to the NEHRP B/C boundary and to Vs_{30} of 760 m s^{-1}, which could be used as representative of Italian NTC18 class-B. However, in-our opinion, the Vs_{30} of 760 m s^{-1} is too close to the boundary between class-A and class-B (800 m s^{-1}). Therefore, here we adopted as representative of NTC18 class-B an amplification curve proposed in Boore & Joyner (1997), and related to Vs_{30} of 520 m s^{-1} as corresponding to NEHRP class-C. Consistently, for NTC18 class-C, we selected the amplification curve proposed in Boore & Joyner (1997) related to Vs_{30} of 255 m s^{-1} (corresponding to NEHRP class-D). Further details can be found in Table 5. Considering the previously mentioned differences between rock conditions in the two seismic codes, for NTC18 class-A, we generated a velocity profile typical for Italian soft rocks (limestones, marls and flysch), without strong impedance contrasts. Similarly, for the four stations lying in NTC18 class-D (corresponding to NEHRP class-E), we produced another curve creating a velocity profile with Vs_{30} in the ranges prescribed by NTC18 (<180 m s^{-1}) and without significant impedance and velocity contrasts. Further details can be found in Table 6. We followed Boore (2003, 2005) using the quarter wavelength approach:

$$A\left(f\left(z\right)\right) = \sqrt{\frac{\rho_S \beta_S}{\bar{Z}\left(f\right)}}, \tag{10}$$

where $\rho_S \beta_S$ is the seismic impedance at the source and $\bar{Z}(f)$ is the average of seismic impedance in a layer with impedance $\rho_z \beta_z$, whose depth $z(f)$ depends on a quarter wavelength:

$$\bar{Z}\left(f\right) = \frac{\int_0^{t(z(f))} \rho_{(z)} \beta_{(z)} \mathrm{d}t}{\int_0^{t(z(f))} \mathrm{d}t}. \tag{11}$$

$$z\left(f\right) = \frac{\bar{\beta}}{4f} \tag{12}$$

In Fig. 4, we show through continuous lines the four curves for $A(f)$ representative, of NTC18 generic site classes (A, B, C and D). According eq. (8), to model the spectral decay at high frequencies in $D(f)$ we used the following values for κ_0:

$$\kappa_0 = \begin{cases} 0.02 \text{ s} & \text{for class} - \text{A} \\ 0.03 \text{ s} & \text{for class} - \text{B} \\ 0.04 \text{ s} & \text{for class} - \text{C} \\ 0.045 \text{ s} & \text{for class} - \text{D} \end{cases} \tag{13}$$

By applying values in eqs (13) to (8), we finally obtained curves for G(f) accounting for both amplification and attenuation contributions. They are plotted in Fig. 4 through dotted lines. The above described values for $A(f)$ and κ_0 were adopted in stochastic simulations for the 133 strong-ground-motion sites, according to each station site class (reported in Table 1).

4 RESULTS

In this section, we discuss the performances of the hybrid ground motion simulations in central Italy computed for the 2016 Amatrice earthquake. At first, to validate the effectiveness of our simulations to reproduce observations, we compare the synthetic hybrid broad-band horizontal-component time histories and Fourier amplitude spectra with the recorded ones at selected strong ground motion stations. Then, we compare the simulated ground-motion parameters with the observed data and the recently published GMPEs. A significant directivity effect has been recognized for this event due to the rupture fault propagation towards NW (Calderoni *et al.* 2017; Lanzano *et al.* 2016; Pischiutta *et al.* 2016; Tinti *et al.* 2016; Luzi *et al.* 2017; Ren *et al.* 2017) for this reason in the following, we distinguish between stations in the forward directivity and in the backward directivity sectors located north and south of the hypocentre, respectively. Discussing about the directivity effects we also examine the less pronounced updip directivity effect observed at near-source at low frequencies causing a pulse-like ground motion at AMT station (Tinti *et al.* 2016). Later, we exploit the same model performing broad-band simulations also for 961 virtual sites, in order to gain insight into the spatial distribution and extent of the strong ground shaking, assessing the spatial distribution of hybrid broad-band PGA and PGV values. Finally, we discuss the contribution of site amplification to the ground motion.

4.1 Synthetic broad-band waveform and Fourier amplitude at selected sites

Synthetic hybrid waveforms in comparison with the strong-ground-motion records are given in Fig. 5, at 4 near-fault stations. Fourier amplitude spectra are shown in Fig. 6 at 12 selected stations. We generally found that our model is successful in explaining amplitude levels and temporal characteristics of observed seismograms. In the Fourier domain recorded spectral amplitudes are generally well reproduced.

Station AMT is the closest station to the fault rupture, with epicentral distance of 9.6 km and Joyner and Boore distance to the fault surface (R_{JB}) of 0.88 km. We simulated PGA of 600 cm s^{-2} and PGV of 29 cm s^{-1}, while observed values ranged from 368 and 851 cm s^{-2} and 41.5 and 43.5 cm s^{-1}, respectively for the two horizontal components. Simulations at NRC at $R_{JB} = 2.67$ km, resulted in PGA of 307.6 cm s^{-2}, while observed valued ranged from 353 and 367 cm s^{-2}; simulated PGV was 19 cm s^{-1}, while observed valued ranged from 24 and 30 cm s^{-1}. Furthermore, synthetic seismic signals well reproduce the source velocity pulse suggesting that the applied hybrid approach is capable to detect near source effects. At station NOR, at $R_{JB} = 2.98$ km simulated PGA is 442 cm s^{-2}, while observed valued ranged from 178 and 200 cm s^{-2}; simulated PGV was 27 cm s^{-1}, while observed valued ranged from 21 and 27 cm s^{-1}. Station RQT ($R_{JB} = 4.63$ km) simulated PGA and PGV are 261 cm s^{-2} and 12 cm s^{-1}, respectively. At this station records were available only for the E-W component, showing observed PGA and PGV of 448 cm s^{-2} and 14 cm s^{-1}, respectively. We finally note that simulated spectra well fit observations in Fig. 6, NOR and SPD being the only two stations showing a

Table 4. Comparison between NEHRP and NTC18 seismic codes regarding the seismic site classification inferred on the basis of Vs_{30} parameter.

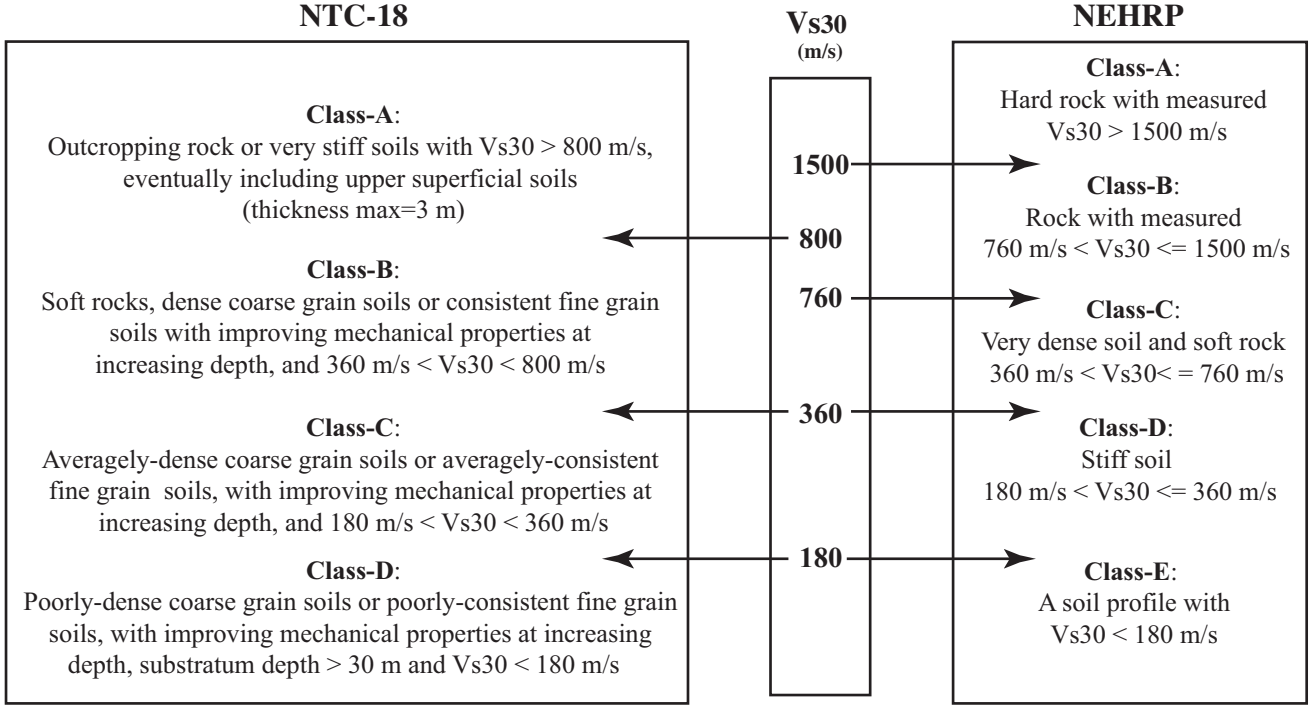

Table 5. Node points of amplification for the site amplification curves adopted in this study for sites B and C according to NTC18 (from Boore & Joyner 1997).

Frequency (Hz)	NTC18 B-Class (from Boore & Joyner 1997, corresponding to NEHRP class C, $Vs_{30} = 520$ m s^{-1}) Amplification	NTC18 C-Class (from Boore & Joyner 1997, corresponding to NEHRP class D, $Vs_{30} = 255$ m s^{-1}) Amplification
0.01	1	1
0.09	1.21	1.21
0.16	1.32	1.32
0.51	1.59	1.59
0.84	1.77	1.77
1.25	1.96	1.96
2.26	2.25	2.25
3.17	2.42	2.42
6.05	2.7	2.7
16.6	3.25	3.25
61.2	4.15	4.15

higher frequency content on simulations than in observed ground motion.

Stations SPD and PCB (class-B site), in the southern side of the fault at comparable Joyner–Boore distances (R_{JB} = 15.6 and 10.1 km), show a general good agreement between simulated and recorded acceleration Fourier amplitude and ground motion levels. Also, at increasing distances simulated acceleration spectrum well fits with observation, as visible on stations MNF (class-A site) and CTD (class-B site), located at increasing distances (R_{JB} = 20.4 and 35.1 km, respectively). Despite the general good consistency, in some cases simulations were not able to reproduce particular features of the observed acceleration spectrum. An example is represented by FEMA (class-B site), in the northern fault side at 13.9 km, where simulations were not able to reproduce a spectral peak at about 2 Hz, prominent on the acceleration spectrum of the EW component.

We also analysed the differences between stations at comparable distances and belonging to different site classes. As an example, in Fig. 6 we report CTD and TRE, at comparable R_{JB} distances. Ground motion levels increase from CTD, belonging to class-B site (simulated PGA = 36.8 cm s^{-2}, PGV = 3.7 cm s^{-1}) to TRE (R_{JB} = 30.2 km; simulated PGA and PGV values 49.2 cm s^{-2} and 5.1 cm s^{-1}), belonging to class-C site, due to the increasing of the site amplification effect. In fact, site class-C is related to lower velocity values in the subsoil that cause amplification. At some stations we finally observed a particular behaviour due to site amplification effects unaccounted in our generic curves. An example is represented by stations AQV and AQK, located at about the same distance and

Table 6. Node points of amplification for the site amplification curves created in this study for sites A and D, according to NTC18.

Frequency (Hz)	NTC18 A-Class created in this study for Italian rock conditions, $Vs_{30} = 1163$ m s^{-1}) Amplification	Frequency (Hz)	NTC18 D-Class created in this study and corresponding to NEHRP class E, $Vs_{30} = 163$ m s^{-1}) Amplification
0.1	1	0.0	1
0.49	1.07	0.1	1.82
0.58	1.1	0.1	2.35
0.68	1.12	0.4	3.21
1.46	1.22	0.4	3.44
2.84	1.33	0.5	3.64
5.1	1.46	1.3	5.05
7.72	1.58	2.7	6.23
9.96	1.68	5.1	6.88
10.8	1.71	7.7	6.99
13.78	1.79	10.0	6.99
15.01	1.82	10.8	6.99
17.42	1.89	13.8	6.99
19.66	1.93	15.0	7
21.1	1.96	17.4	7
22.9	1.98	19.7	7
31.59	2.09	21.1	7
36.53	2.13	22.9	7
58.33	2.2	31.6	7

classified as a class-B soil category. At station AQV ($R_{JB} = 28.9$ km) observed ground motion is quite well reproduced both in frequency (see Fig. 6) and time domain (simulated PGA = 55.7 cm s^{-2}, PGA = 4.7 cm s^{-1}; observed PGA between 45.3 and 59.6 cm s^{-2}, PGV between 3.9 and 4.4 cm s^{-1}). Conversely, at station AQK ($R_{JB} = 33.9$ km) simulations are not able to capture a low frequency amplification peak at about 0.8 Hz, recognized in literature as due to a well-known impedance contrast occurring at depth larger than 30 m in a sedimentary basin (e.g. De Luca *et al.* 2005; Akinci *et al.* 2010; Puglia *et al.* 2011). This results in underestimating simulated ground motion (simulated PGA = 45.2 cm s^{-2}, PGV = 4.6 cm s^{-1}; observed PGA between 49.5 and 57 cm s^{-2}, PGV between 9 and 9.8 cm s^{-1}), especially on velocity that is more sensitive to low frequencies.

4.2 Residuals between observed and simulated values

To get an insight on simulation reliability, we calculated residuals R_{OSj}between observed and simulated values at each distance R_{JB}, related to station j as:

$$R_{OSj}\left(T_j\right) = \log 10\left(\frac{Y\left(T_j\right) j, OBS}{\bar{Y}\left(T_j\right) j, SIM}\right), \quad (14)$$

where Y is the observed ground motion parameter (PGA, PGV), and $\bar{Y}$ is the one derived from hybrid broad-band simulation.

Residuals between observed and simulated ground motion parameters, PGA and PGV (PSA at 0.3 and 1 s can be found in the Supporting Information of this paper, Fig. S1) are plotted in Fig. 7, separating EW and NS components of ground motion. We also distinguish between stations in the forward directivity (black) and in the backward (grey) directivity sectors. The symbol refers to the subsoil site class. We observed that for the most of the stations, the residuals vary between [–0.5 0.5], suggesting that our model is able to adequately reproduce observed ground motion levels both in PGA and in PGV.

From this figure we are not able to infer a clear pattern of forward and backward directivity sectors suggesting that our broad-band hybrid model contains some directivity content. Besides, PGA and PGV data do not show the same distribution of coloured symbol, preventing us to interpret the results in terms of directivity only by using this figure. The largest variation of R_{OS} ratio is observed between 30 and 100 km, where most of the stations are located.

To quantify these residuals and to compare the performance of our hybrid model with those observed with GMPEs, we computed the bias of the model used for the simulations averaging over the sites, the logarithm (base 10) of the ratio of the observed to the simulated in terms of PGA and PGV parameters.

For the hybrid simulation model, the average value is estimated as 0.06. We also calculated the standard deviation over all the ground motion parameters derived from the residuals between simulations and observed data and obtained as 0.25.

We will see in the following section 4.3 that these values (model bias and standard deviation) are smaller than those calculated for the GMPE models.

4.3 Comparison with ground motion prediction equations

In this section we compare the simulated hybrid broad-band accelerations and velocities with two different commonly used GMPEs for the active shallow crustal regions. These include the GMPE developed within the context of the Next Generation Attenuation (NGA) models by Boore *et al.* (2014; hereafter, BSSAA14) and the Italian model of Bindi *et al.* (2011; herafter, ITA10). The selected GMPEs were derived from the normal-faulting style and for three site conditions related to NTC18 classes-A, -B, -C and -D, respectively.

In Fig. 8, we show the simulated hybrid broad-band PGAs, PGVs (PSA at 0.3, 1 and 2 s are given in the Supporting Information, Fig. S2), up to 150 km as a function of R_{JB} for the 133 seismic

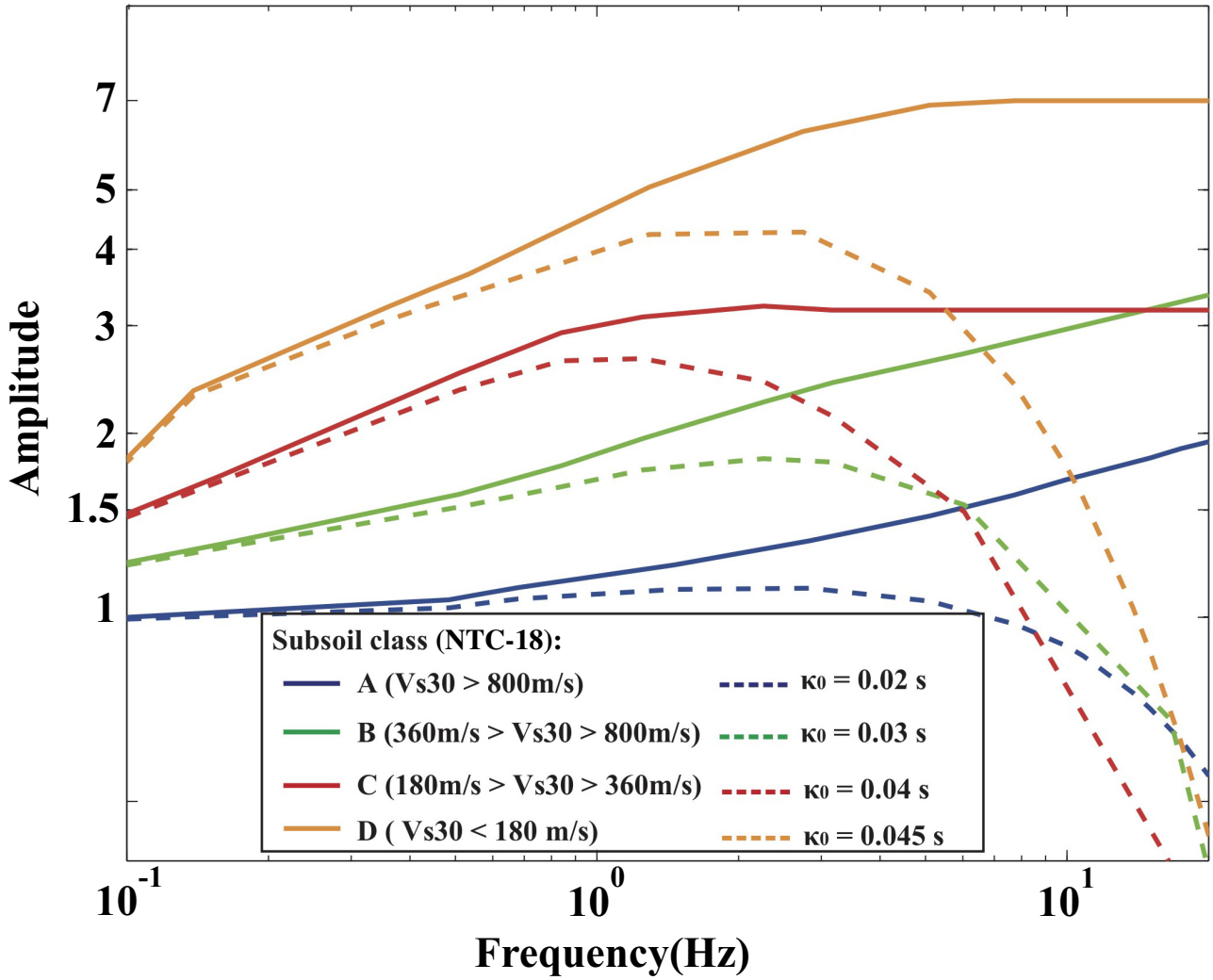

Figure 4. Site amplification curves adopted in this study without attenuation (solid lines) and including attenuation for different values of the k_0 coefficient (dotted lines).

stations. The observed ground motion and the above-mentioned GMPEs together with their $\pm\sigma$ standard deviations are plotted as well. Both observed and simulated ground motion parameters do not fall into the one standard deviation range of the GMPEs presented with different soil category. As it is seen in Fig. 8, the observed ground motions show large variability and highly scattered data over all the distance ranges, presenting a complicated anatomy that might be aggregated by several factors pertinent to the source, propagation and site effects. It is observed that the simulated ground motions are in close agreement with observations. The Italian GMPE, ITA10 underestimates the observed PGAs especially those recorded on the bedrock (site class-A); nevertheless, it provides better fit compared to the BSSA14 GMPE, both for the PGA and PGV ground motion parameters.

In order to assess the level of fit between our simulations and GMPEs, we calculated residuals R_{SGj} at each R_{JB}, j as:

$$R_{SGj}\left(T_j\right) = \log 10\left(\frac{\bar{Y}\left(T_j\right) j, SIM}{Z\left(T_j\right) j, GMPE}\right), \tag{15}$$

where $\bar{Y}$ is the considered parameter (PGA, PGV) from hybrid broad-band simulation, and Z is the one calculated from GMPEs. Residual calculation was performed only for the two GMPEs considering the site class (ITA10 and BSSA14), each station being compared with the GMPEs calculated for the corresponding soil site category.

Fig. 9 shows the plots of PGA and PGV residuals (PSA residuals can be found in the Supporting Information of this paper, Fig. S3) versus the distance to evaluate the agreement with the selected GMPEs. Symbols colour represents the GMPE used in residual calculation (red and blue for comparison with ITA10 and BSSA14, respectively). PGA and PGV residuals principally fall between –0.5 and 0.5 of the ITA10 empirical equation. Figs 9(a) and (b) show that the broad-band simulations accommodate the GMPEs with reasonable trend, where the perfect fit would result in zero R_{SG} whereas negative residuals indicate an underestimation of the simulations with respect to the empirical model from GMPEs. At all distances and particularly for PGA, ground motion parameters better agree with ITA10 than with BSSA14. Although the PGA and PGV residuals principally fall between –0.5 and 0.5 for both GMEPs, the overestimation of BSSA14 is higher at increasing distances. Moreover, the overestimation of BSSA14 is also higher for stations belonging to B and C soil classes (see Fig. 8). The standard deviations are

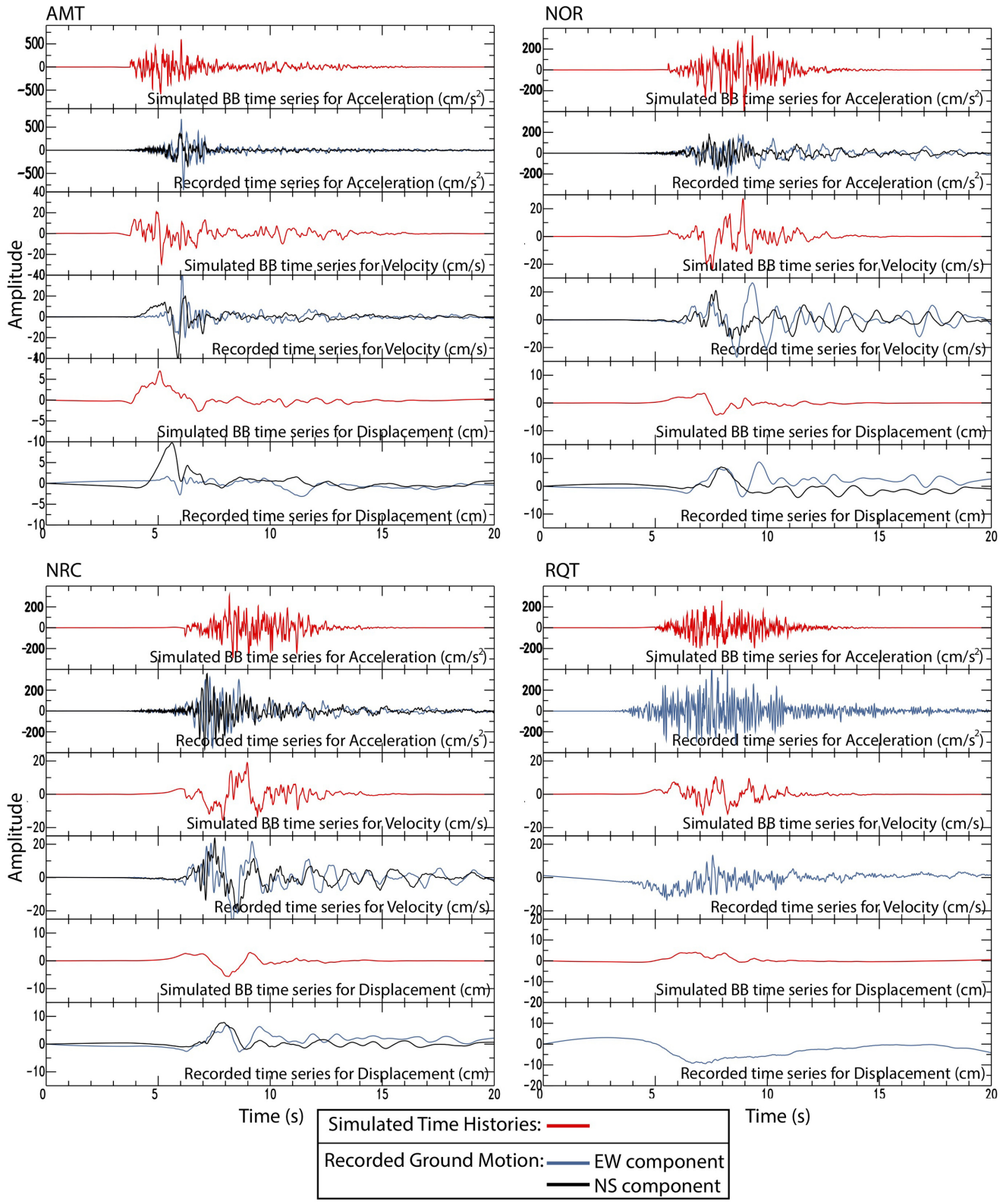

Figure 5. Hybrid broad-band simulated time histories at near-fault stations, obtained using Tinti *et al.* (2016) slip model and high frequency stochastic simulations (red). Recorded horizontal ground motion data are reported as well (black and blue for NS and EW components, respectively).

calculated as 0.23 and 0.38 for PGA and PGV residuals evoked between simulated and ITA10 model, while the standard deviation results 0.48 and 0.36 in the case of the BSSA14, respectively, for PGA and PGV.

Following the Al Atik *et al.* (2010), we calculate the event- and site-corrected residuals subtracting the distance mean residuals calculated over four distance ranges (0–20, 0–50, 50–100 and 100–150 km) from the total residuals. In Figs 9(a) and (b) the large

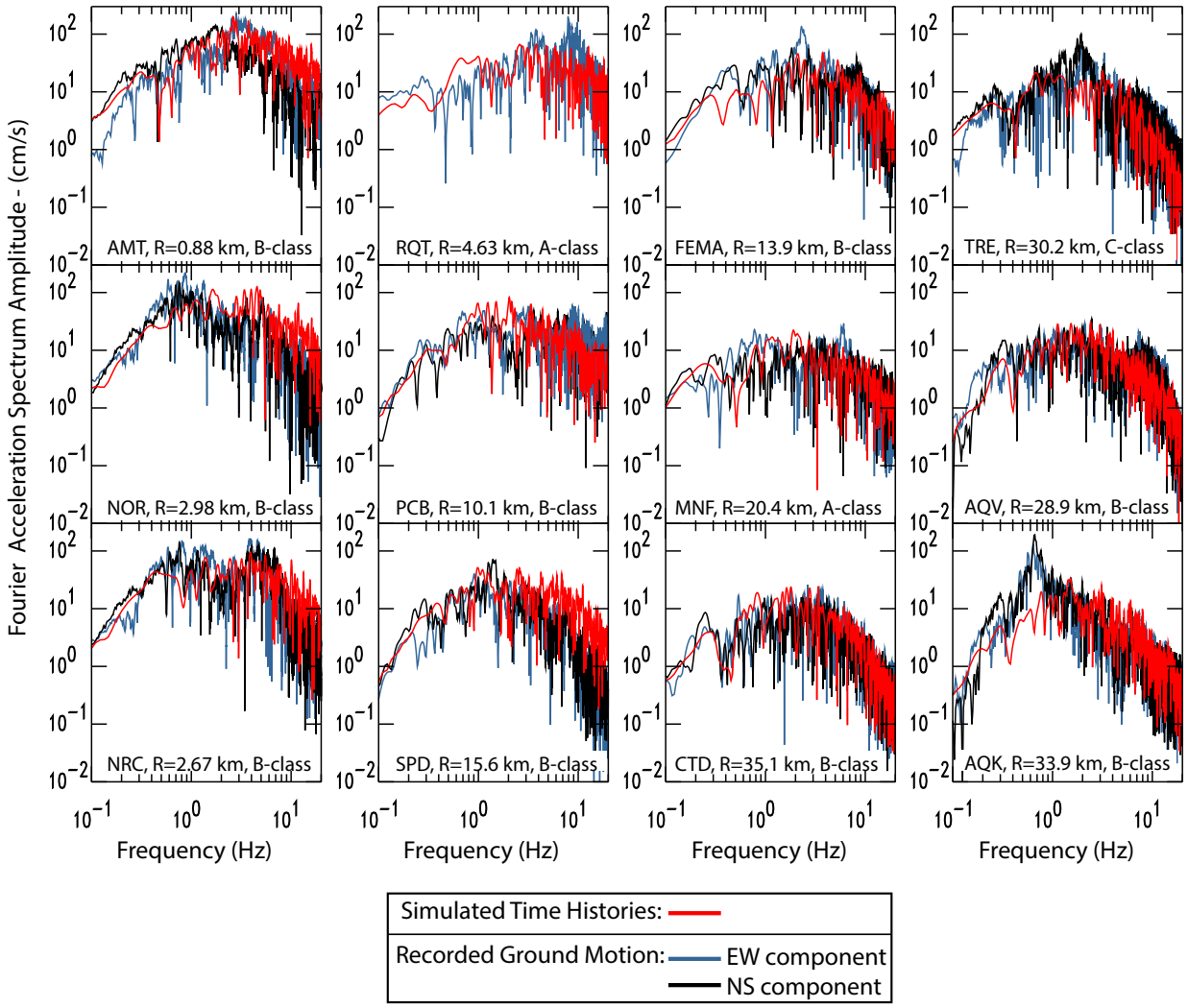

Figure 6. Fourier amplitude spectra at 12 selected stations related to broad-band synthetic signals obtained using Tinti *et al.* (2016) slip model and high frequency stochastic simulations (red). Fourier spectra from recorded horizontal ground motion data are reported as well (black and blue for NS and EW components, respectively).

yellow and light blue squares with error bars present the means of the total residuals over the four distance ranges (0–20, 20–50, 50–100 and 100–150 km) for ITA10 and BSS14, respectively. In Figs 9(c) and (d) we show the path corrected residual to investigate the spatial variation of the observed ground motions versus GMPEs.

In order to make a further comparison we also calculated residuals between observed ground motion parameters and the ones predicted by GMPEs, R_{OGj} at each R_{JB}, j as:

$$R_{OGj}\left(T_j\right) = \log 10\left(\frac{\bar{Y}\left(T_j\right) j, OBS}{Z\left(T_j\right) j, GMPE}\right), \tag{16}$$

where $\bar{Y}$ is the observed ground parameter (PGA, PGV), and Z is the one calculated from GMPEs. The R_{OGj} residuals are presented in Figs 10(a) and (b), their distribution ranging from –1 and 1. The same residuals calculated on PSAs are provided in the Supporting Information (Fig. S4). Residuals R_{OGj} are generally higher than R_{SGj} due to site or directivity effects not properly reproduced by the empirical equations. Consistently to residuals R_{SGj}, ground motion parameters better agree with ITA10 GMPE than with BSSA14. The total standard deviation, between observed and GMPE models, calculated over all the ground motion parameters (PGA, PGV and SAs at 0.3, 1 and 2 s) is 0.32 and 0.37 for ITA10 and BSSA14 empirical models, respectively, while it is smaller (0.25) for the hybrid simulation model. For that reason, we preferred to use only Italian GMPE ITA10 empirical model in the next sections for further considerations.

Consistently to Figs 9(c) and (d), in Figs 10(c) and (d) we show the path corrected residual calculated according to Al Atik *et al.* (2010), to investigate the spatial variation of the observed ground motions versus GMPEs.

From Figs 7 and 10 we observe that the calculated residuals between simulated and recorded data demonstrate less variability with distances whereas the residuals calculated between recorded data and the GMPEs are much more scattered. To quantify these latter residuals, we compute the bias estimated from the GMPE model (averaging the values of ground motion parameters over the sites and distance bins) and it resulted 0.11, which is larger than the bias estimated for the hybrid model, 0.06 in the previous section.

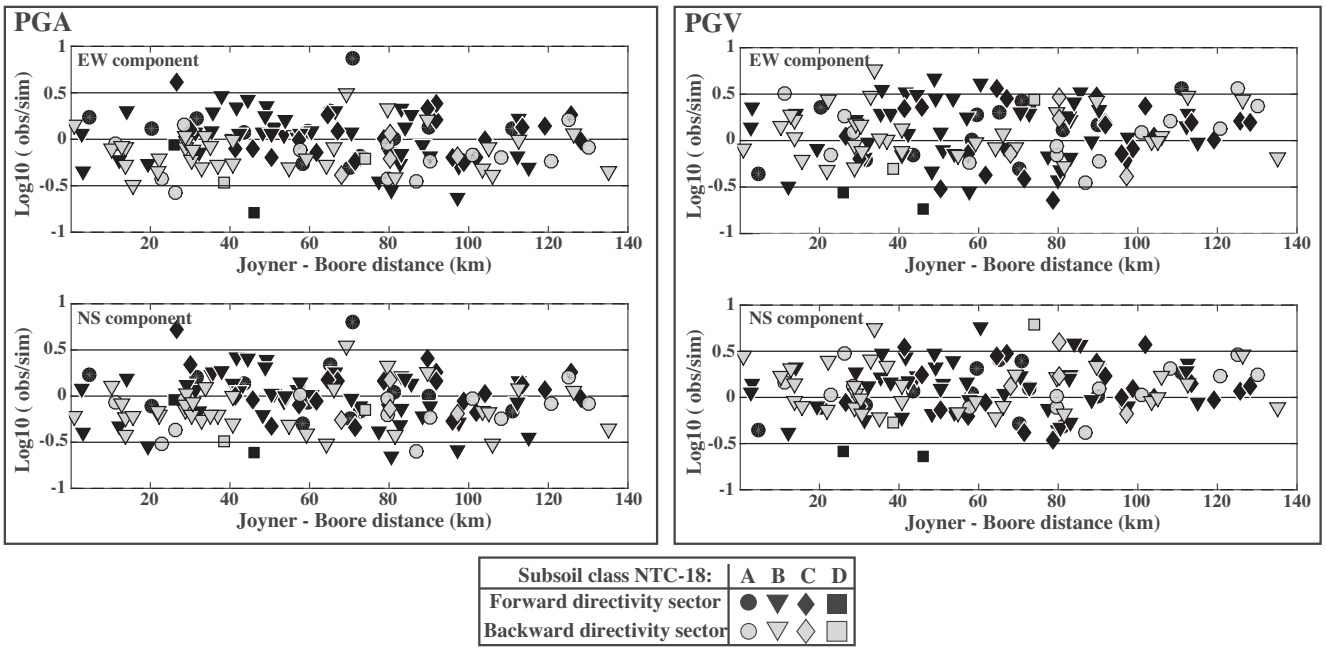

Figure 7. Residuals between ground motion parameters observed on data recordings and simulated broad-band time-series: peak ground acceleration (PGA) and peak ground velocity (PGV). PSAs residuals are provided in the Supporting Information (Fig. S1).

As mentioned previously the total standard deviation calculated over all the ground motion parameters is larger for the ITA10 and BSSA14 GMPE models, while it decreases for the hybrid simulation model. All these results indicated that simulated ground motion parameters better mimic the observed data than those of the GMPEs.

4.4 Spatial distribution of ground motion from hybrid broad-band simulation

Using the simulation technique described here, we simulated bedrock ground motion at a dense grid of virtual receivers in the epicentral region. Synthetic ground motion was generated at 961 virtual sites along a regular grid size of 5 km × 5 km covering the study area (42–43.5°N, 12.5–14°E). The occurrence of site-amplification effects was not included in this model so that the predicted ground-motion levels refer to generic conditions corresponding to the site class-B of the Italian seismic code NTC18. PGA and PGV (PSA maps can be found in the Supporting Information of this paper, Fig. S5) values are assessed to get an insight into the spatial distribution and extent of the strong ground shaking. The horizontal peak ground-motion distributions for PGA and PGV are shown in Fig. 11. We observed that the largest ground shaking is obtained along the rupture fault plane, PGA and PGV values reaching about 1.5 g and 65 cm s^{-1}, respectively. In particular, PGAs and PGVs distributions show that the strongest ground shaking is observed around the location of the two large-slip asperities. In particular, the directivity pattern caused by the updip propagation is become evident only around the surface exposure or around its updip projection (Somerville 2003). These updip effects, without stations right on top of the rupture (as AMT station) are very difficult to be observed (Ross *et al.* 2020). However, in Fig. S5(c) we show this similar feature in near source at intermediate frequencies.

Finally, while the near-field results are governed by the source effects, such as the distribution of asperities on the fault plane, intermediate distances are controlled by path effect, the seismic wave propagation and the attenuation of seismic waves.

4.5 Investigating the rupture directivity effect from observed, simulated and GMPEs data

Through the analysis of the instrumental data several authors observed an evident forward directivity effect caused by the fast rupture propagation towards NW direction along the seismogenic fault (Calderoni *et al.* 2017; Lanzano *et al.* 2016; Spagnuolo *et al.* 2016; Luzi *et al.* 2017; Ren *et al.* 2017). Here in order to get insight into the capability of simulations in reproducing such directivity effect, we discuss the residuals between observed (EW component) and simulated ground motion parameters as well as the ones predicted by the empirical model and plotted for PGA and PGV shown in map view in Figs 12(a)–(d). The same residuals calculated using the recorded NS component are given in the Supporting Information (Fig. S6).

The path- and site-corrected residuals between observed ground motion parameters and the ones predicted by Italian GMPEs, ITA10, R_{OG} (eq. 16) are presented in Figs 12(a) and (b) for both ground motion parameters. As it is seen in the figure, positive residuals (hot colours) are observed in the forward directivity areas (in the northwest side) where observed ground motion parameters are underestimated by GMPEs. Conversely, negative residuals (cold colours) are observed in the back-forward directivity regions (in the southeast side), indicating overestimation of observed values by GMPEs. Luzi *et al.* (2017) and Lanzano *et al.* (2016) have calculated the site- and event-corrected residuals, using the GMPE as a reference, and observed largest ground-motion variability in the direction parallel to the fault strike, referring this variation to the rupture directivity. Our results are in agreement with their findings regarding the fault rupture features of the Amatrice earthquake.

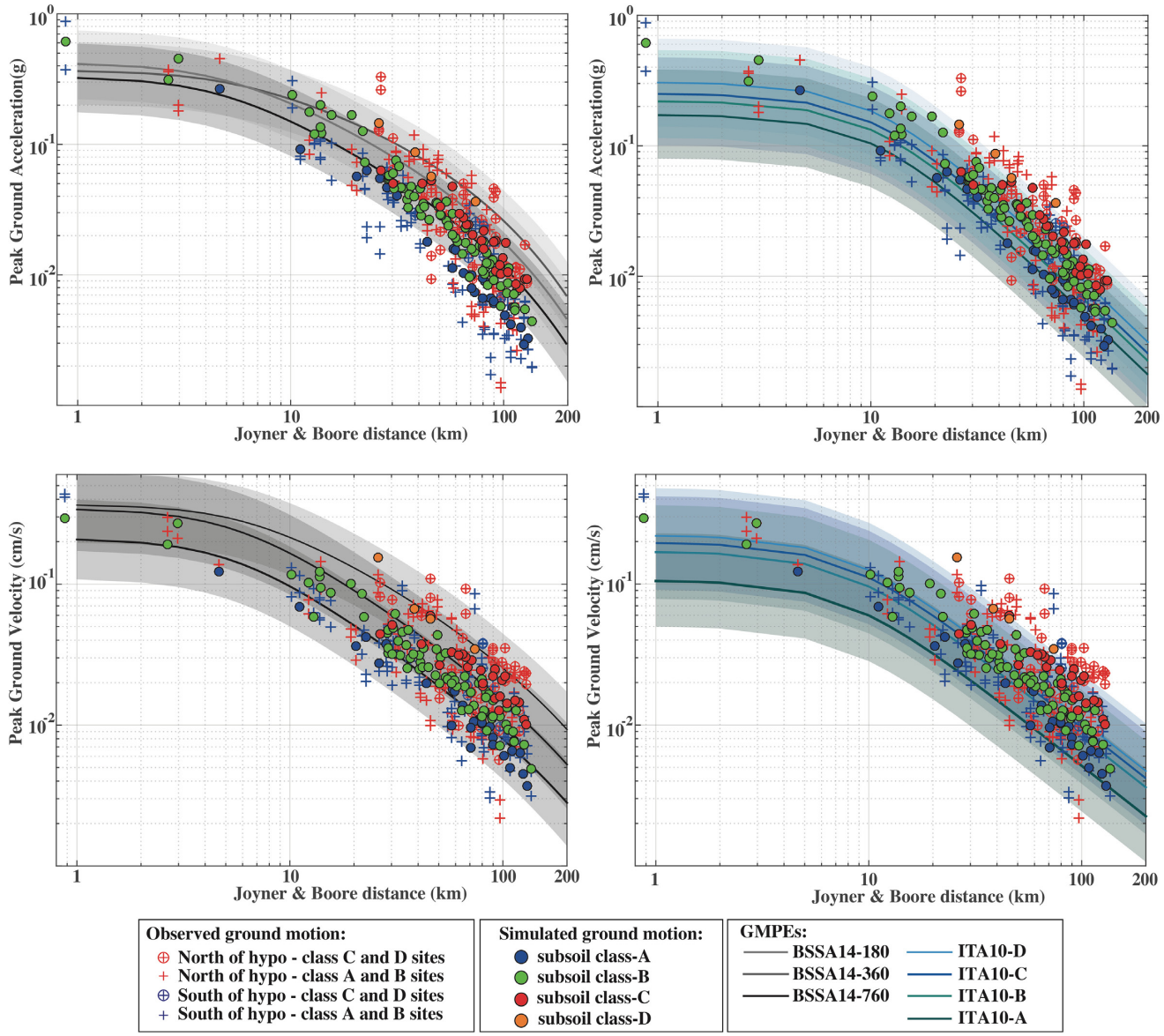

Figure 8. Ground motion parameters (PGA and PGV) of hybrid broad-band synthetics related to the considered stations and using Tinti *et al.* (2016) slip model. PSAs are given in the Supporting Information (Fig. S2). Symbol colour is related to the seismic site class according to NTC18. In left-hand panels we show comparison with the following ground-motion predictive equations (GMPEs): GMPEs developed within context of the Next Generation Attenuation (NGA) models project, Boore *et al.* (2014; hereafter, BA2014). In right-hand panel we show comparison with GMPEs by the Italian model of Bindi *et al.* (2011; hereafter, ITA10). The recorded values on the two horizontal components at the seismic stations are reported as well (crosses).

We also highlight that at AMT station, even if it is located in the southern sector, is underestimated by GMPEs. This is in agreement with the secondary directivity effect discussed in Tinti *et al.* (2016) caused by the slip patch located just above the hypocentre.

Similarly, in Figs 12(c) and (d) we show the spatial variations of the residuals between observed and simulated ground motions R_{OS} (eq. 14). We noted that the spatial variations of residuals for PGA and PGV parameters, calculated between observed and simulated are similar to the residuals computed between observed and GMPEs, where the northern and southern areas were under and overestimated, respectively. Although the directivity effect has been introduced in the hybrid simulation up to 1 Hz as observed at two stations near-source (AMT and NRC), the stochastic high frequency content of the simulations seems not to reveal this signature. In Fig. S7, we show the spatial variations of the residuals of PGA and PGV parameters between simulated ground motions and GMPEs R_{GS} (eq. 15). Consistently to Figs 12(a), (b), in Fig. S7 positive residuals (even being less pronounced) are mainly observed in the forward directivity areas while negative residuals are mostly observed in the southern part of the fault projection.

In Fig. 13, we show some acceleration response spectra at 5 per cent damping ratio, using a linear scale. In the Supporting Information (Fig. S8) they are graphed using a log–log scale.

Acceleration spectra are shown comparing simulated (thick line) and recorded signals (thin lines, solid and dashed for NS and EW, respectively) at pairs of stations, selected considering similar R_{JB} distance ranges and the same site class. Comparison between spectral acceleration at stations NRC and AMT, located at similar distances from the fault projection but in opposite

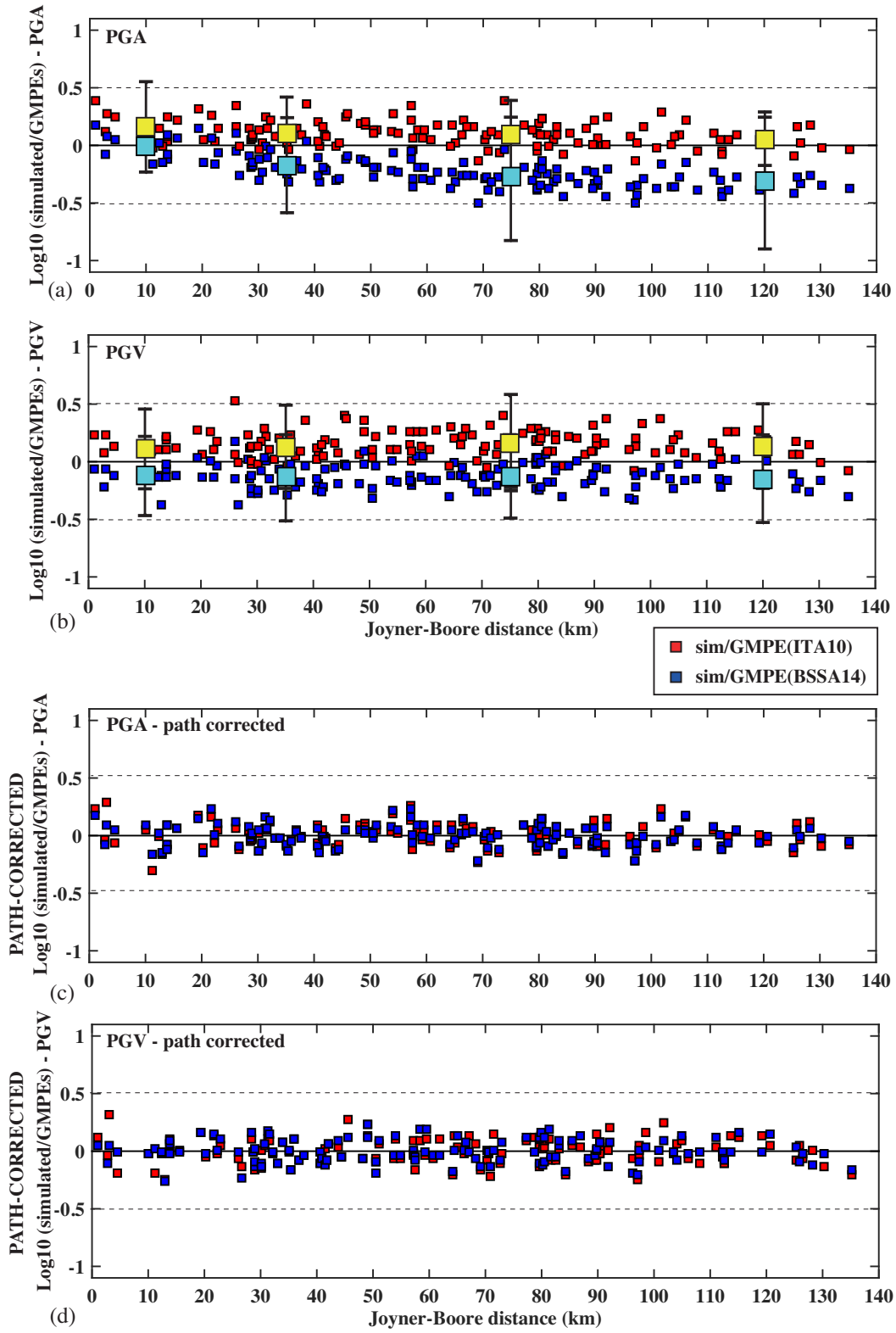

Figure 9. Total residuals between values of simulated ground motion parameters and the expected ones according to GMPEs (BSSA14 and ITA10) for ground motion parameters PGA in panel (a) and PGV in panel (b). The large yellow and light blue squares with error bars present the mean residuals of the total residuals over the four distance ranges (0–20, 20–50, 50–100 and 100–150 km) for ITA10 and BSSA14, respectively. Residuals are then calculated applying the path correction in order to investigate the ground motion variability in the study region (PGA in panel c) and PGV in panel d). PSAs total residuals are provided in the Supporting Information (Fig. S3).

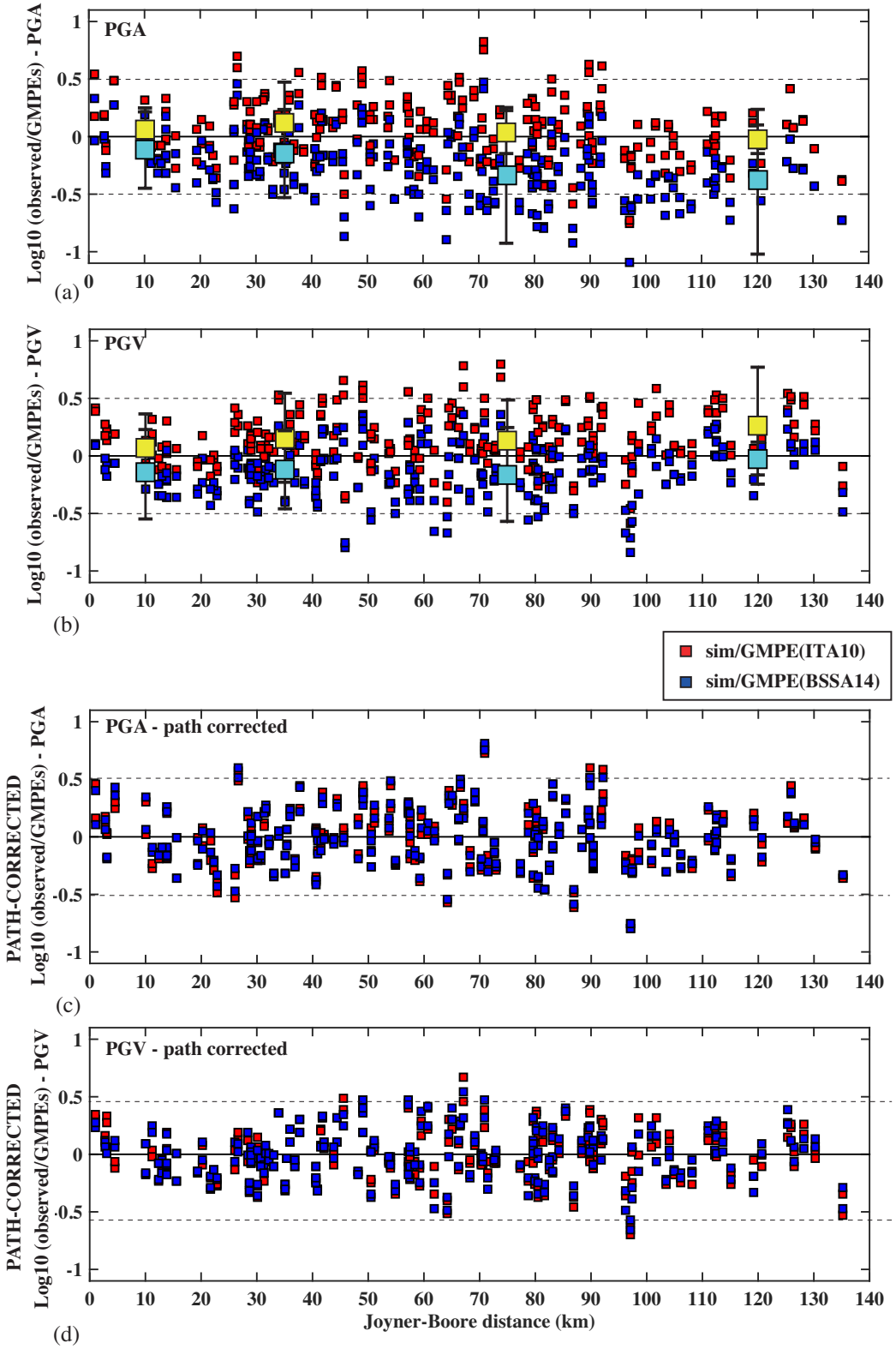

Figure 10. Total residuals between values of recorded ground motion parameters and the expected ones according to GMPEs (BSSA14 and ITA10) for ground motion parameters PGA in panel (a) and PGV in panel (b). The large yellow and light blue squares with error bars present the mean residuals of the total residuals over the four distance ranges (0–20, 20–50, 50–100 and 100–150 km) for ITA10 and BSSA14, respectively. Residuals are then calculated applying the path correction in order to investigate the ground motion variability in the study region (PGA in panel c) and PGV in panel (d). PSAs total residuals are provided in the Supporting Information (Fig. S4).

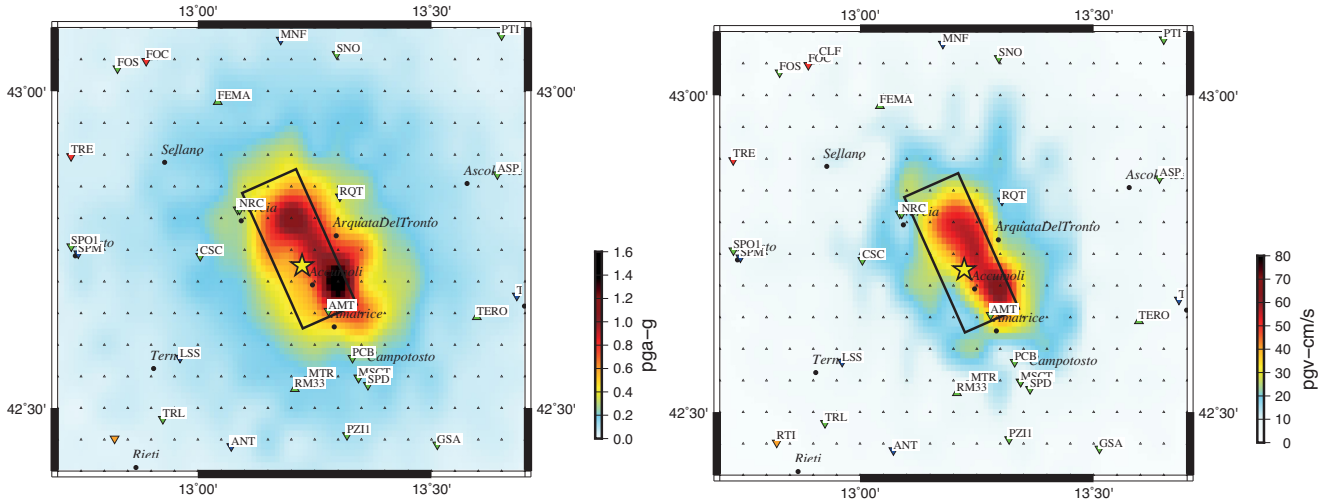

Figure 11. Spatial distributions of broad-band ground motion (hybrid horizontal component) at 961 virtual stations located following a regular grid spacing of 0.5 km × 0.5 km, in terms of peak ground acceleration (PGA, g), peak ground velocity (PGV, cm s^{-1}). PSAs at 0.3, 1 and 2 s are given in the Supporting Information (Fig. S5). Simulations were performed using the parameters given in Table 2.

positions from the epicentre, indicates that, in the near source, AMT presents larger spectral acceleration than NRC for both observed and simulated signals. Despite the expected directivity toward north, this large acceleration observed at AMT indicates the signature of the less pronounced directivity due to the updip rupture, in agreement with the results presented by Tinti *et al.* (2016).

Stations FEMA, MNF, MTL and TLN, located at intermediate distances towards north, show higher response spectra on recordings respect to the stations SPD, ANT, PGG and FMG with similar distances and site properties but located at the opposite site of the rupture propagation (back forward directivity). However, at many pairs of stations in Fig. 13 (SPD-FEMA; ANT-FOS; FMG-TLN; PGG-MTL) the tendency of higher ground motion in the forward directivity sector observed on recordings is not fully reproduced by our simulations particularly at high frequencies. The spectral accelerations of the simulated seismograms are much more similar among each other in the TLN-FMG, MTL-PGG pairs of stations regardless of their azimuthal distributions (Fig. 13, red and black thick lines) suggesting a limitation of our hybrid procedure in completely capturing the source directivity effects.

4.6 The role of site amplification and limitations of the followed approach

In Section 3.1.3 we attempted to explain the method chosen to include site amplification in our stochastic simulations. We used amplification curves for the different site classes (Fig. 4) as prescribed by Italian NTC18 seismic design code: class-A, -B, -C and -D (Table 4). Specifically we choose to use two amplification curves proposed by Boore & Joyner (1997) for sites B and C, and to generate by our-own an amplification curve for sites A and D through the quarter wavelength approach (Boore 2003, 2005).

As a whole, this approach has certainly improved the fit between observed and simulated time histories and ground motion levels. However, there are several sites where the use of generic curves is not enough adequate, simulations underestimate or overestimate the recorded ground motion. In fact, generic curves do not consider specific geological features and particular site-conditions, as for example impedance contrasts in sedimentary basins and, in general, velocity and impedance contrasts generated by the site-characteristic stratigraphy.

An example is represented by station AQK, located close to L'Aquila, in a sedimentary basin filled by lacustrine sediments with a maximum depth of about 250 m. A relevant site amplification effect was reported in literature by previous papers (e.g. De Luca *et al.* 2005; Di Giulio *et al.* 2014; Amoroso *et al.* 2018). It was observed at low frequencies (0.6 Hz), associated to very long durations in the coda of seismic records. By comparing simulation Fourier spectra (Fig. 6) and spectral acceleration at stations AQV, AQF and AQK (located at about the same R_{JB} distance and all in the site class-B), we found that at station AQK simulations strongly underestimate observation, being unable to reproduce the low frequency amplification at about 0.6 Hz.

In order to achieve a better fit between observed and simulated ground motion, we tested the use of amplification curves derived from recorded ground motion, rather than exploiting the generic ones derived from NTC18 classes, as described in the previous section. At ten selected sites, as an amplification term (eq. 10) adopted in the stochastic high frequency calculations we applied the HVRS (horizontal-to vertical response spectra) curve provided in ITACA 3.0 database (http://itaca.mi.ingv.it/ItacaNet_30/#/home) for each station. Information about geology, velocity profile and available geophysical prospecting are provided too.

We also tested the application of the HVRS as well as HVSR (horizontal-to-vertical spectral ratios), calculated separately at each station. For some of them, they were calculated in this work using seismic events downloaded from the database (shown in Fig. 14a), for other stations they were available on the ITACA database.

In Fig. 14(a) we showed velocity Fourier spectra and time histories derived from the use of different amplification curves in the calculations: the generic amplification curve assigned on the basis of the soil classification according to Italian seismic code NTC18 (see Section 3.1.3); the means of HVRSs provided in ITACA database; the means of HVSRs calculated in this work using seismic events downloaded by ITACA database.

We have found some interesting features at three stations in L'Aquila intermountain sedimentary basin. Even if they all fall in

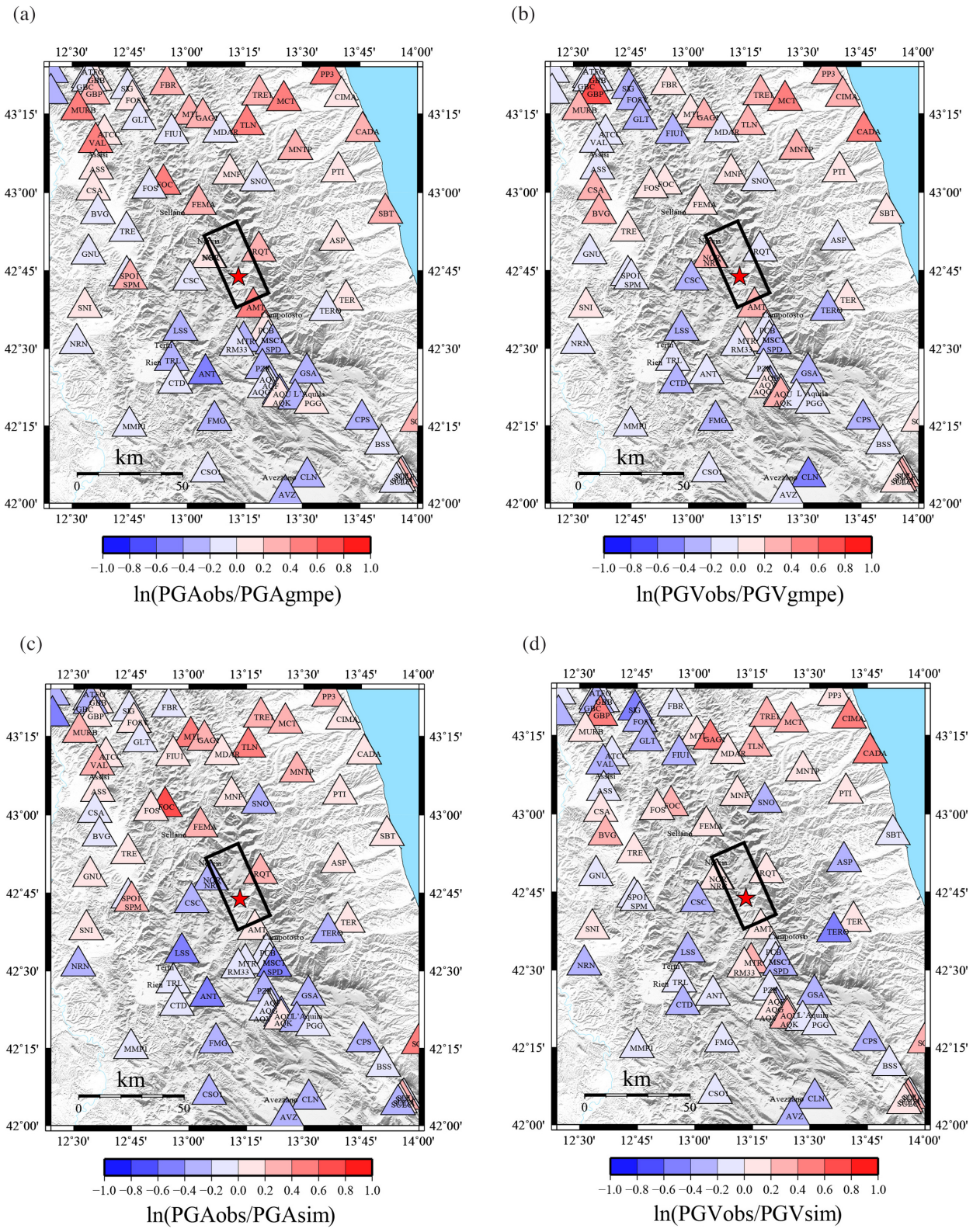

Figure 12. Spatial distributions of the path-corrected residuals for investigating the directivity effect of the ground motion parameters (a) PGAs and (b) PGVs using the Italian model of Bindi *et al.* (2011) and the observed data (for the EW component, and the NS component presented in the Supporting Information, Fig. S6); (c) the spatial distributions of PGAs and (d) PGVs residuals calculated between observed and simulated data. The triangles indicate the strong motion station locations, hot colour indicates sites that are overestimated while cold colour demonstrates the stations are underestimated by the GMPEs and simulated data.

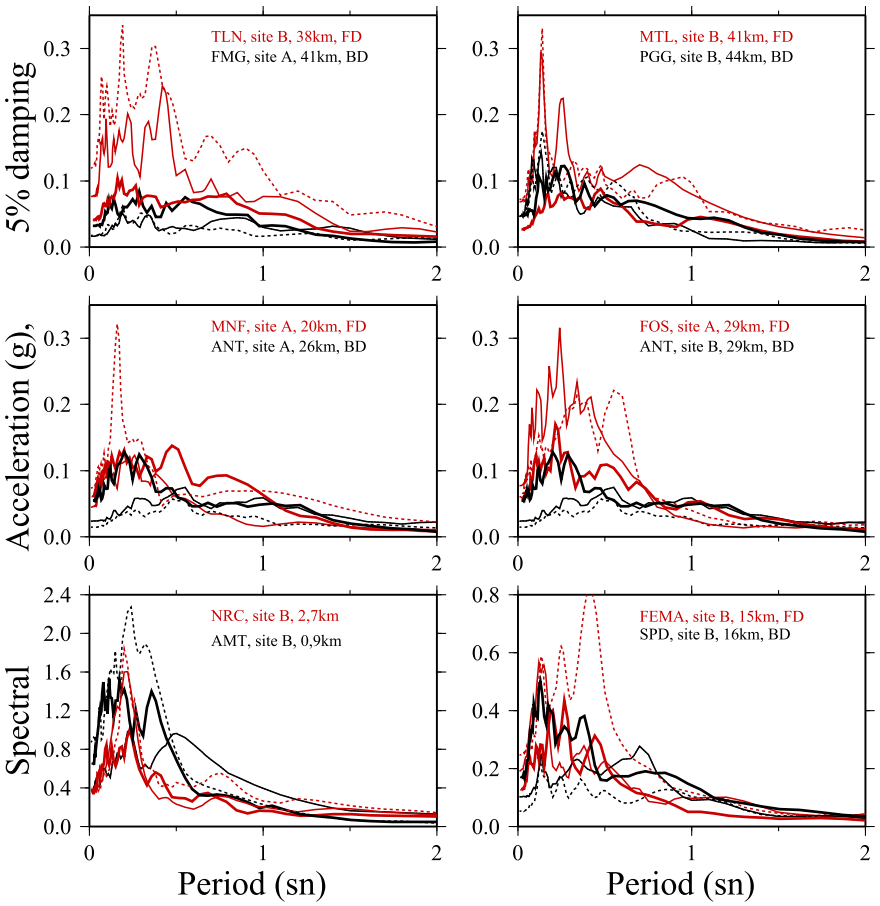

Figure 13. Acceleration response spectra at 5 per cent damping for simulated and recorded signals in a lin–log scale. They are provided in a log–log scale in the Supporting Information (Fig. S8). Pairs of stations are selected considering similar R_{JB} distance ranges, as well as the site class. We distinct recorded acceleration response spectra (dashed thin lines for EW components, solid thin lines for NS components) in forward directivity (red thin lines, FD) and backward directivity sectors (black thin lines, BD). Similarly, simulated response spectra are shown in forward directivity (red thick lines) and backward directivity sectors (black thick lines) as well.

the NTC18 class-B (since they have mean shear wave velocity in the first 30 m depth ranging from 360 to 800 m s^{-1}), their geological and geotechnical setting, as well as velocity distribution at depth is very different. Station AQG is installed on mudstone and marls, with no significant velocity contrasts up to 35 m. Both HVRSs and HVSRs show an amplitude 4 peak at about 5 Hz. Station AQV is located close to the border of the basin, showing a velocity contrast at roughly 50 m, which causes two resonance peaks at 3 and 10 Hz, with amplitude from 4 to 6. We remark that amplitudes are slightly lower on HVRSs than HVSRs, as an effect of the instrument damping. Finally, station AQK (previously mentioned in section 5) is located in the middle of a sedimentary basin show an amplitude 3 peak at about 0.6 Hz on HVRSs. They underestimate amplitudes observed on HVSRs and published in De Luca *et al.* (2005), reaching over 6 in the same frequency band. The velocity down-hole measurements did not reach the depth of the impedance contrast, reaching a depth of 50 m only. Simulated hybrid broad-band spectra and time histories at stations AQV and AQG do not change significantly by using different amplification terms. Conversely, at station AQK the use of HVRSs and HVSRs allows to reproduce the amplification peak observed on data at about 0.6 Hz. We stress that using the generic site curve based on the Vs_{30} parameter (i.e. the site class prescribed by design code NTC18) we were not able to reproduce this peak. This limitation is also intrinsic in the use of the Vs_{30} parameter adopted in our computations as well as in design codes, which is insensitive to at depth higher than 30 m, being unable to capture peaks produced by impedance contrasts at depths higher than 30 m.

Station CLF is located in Colfiorito sedimentary basin and belongs to NTC18 class-D. HVRSs published on the ITACA database reveal amplitude 6 peaks at about 1 Hz, probably caused by an mpedance and velocity contrast found on borehole investigations at 54 m. This is in agreement with findings published by Di Giulio *et al.* (2006). At this station we found that, even if the use of recorded HVRSs and HVSRs led to a better match between observed and simulated spectra at low frequencies, recorded PGV is always higher than simulated. This could be ascribed to 3D amplification effects caused by the geometry of the impedance contrast between soft sediments and underlying rock formations, and by wave reverberation across the sedimentary body. Such effects cannot be modelled with the stochastic wave propagation approach.

Stations AVZ and BTT2, located in Fucino sedimentary basin and belonging respectively to class-C and -D, represent another example of 3-D reverberation across a sedimentary basin. While the former is located close to the basin border (characterized by an amplitude 3–6 peak at 0.7 Hz on HVRSs and HVSRs), the latter is located in the middle of the basin, and is characterized by

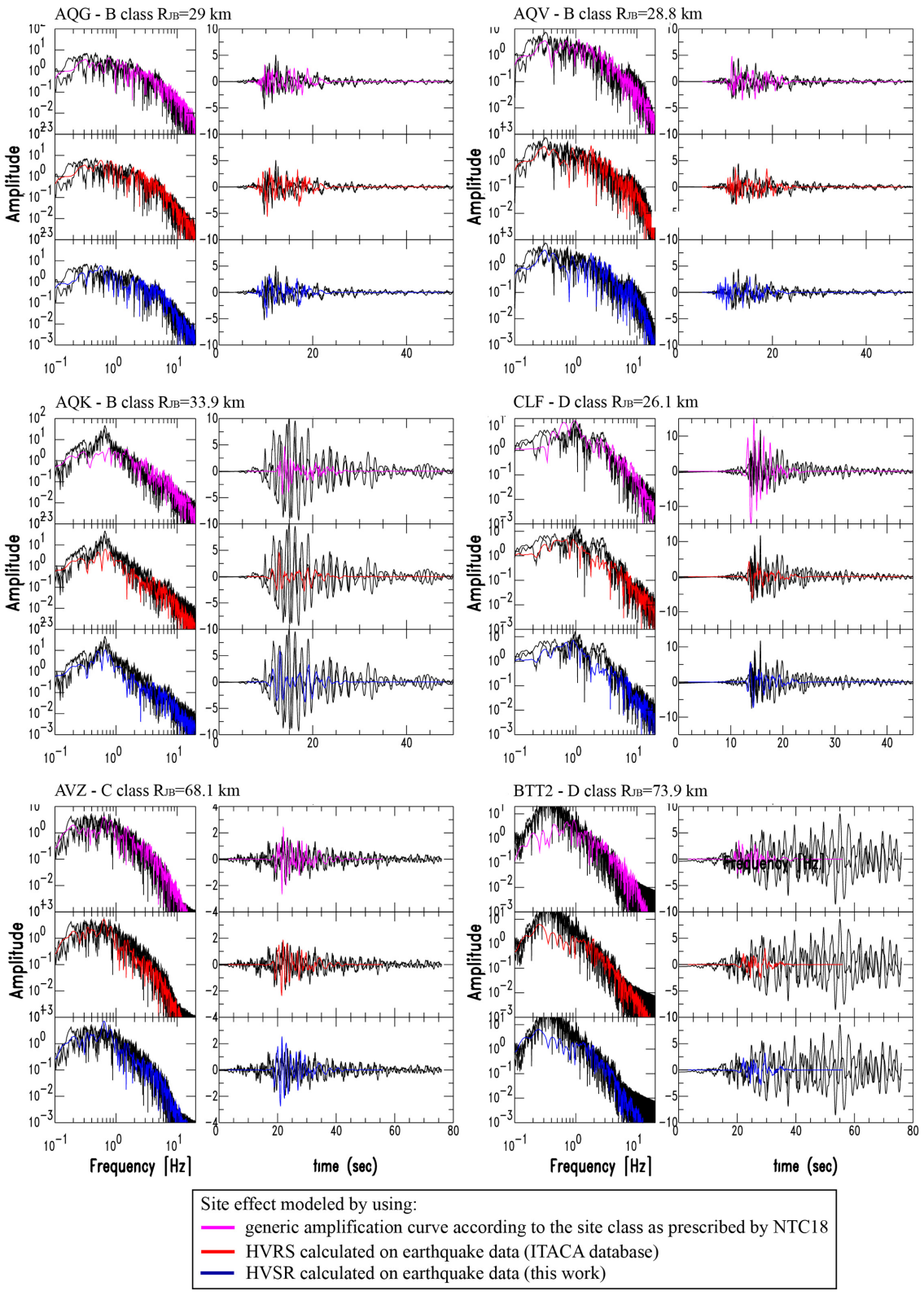

Figure 14. (a) Velocity amplitude spectra and broad-band simulated time histories obtained by using different amplitude curves to include the site effect in stochastic simulations at six representative stations. (b) Velocity amplitude spectra and broad-band simulated time obtained by using different amplitude curves to include the site effect in stochastic simulations histories at 4 representative stations.

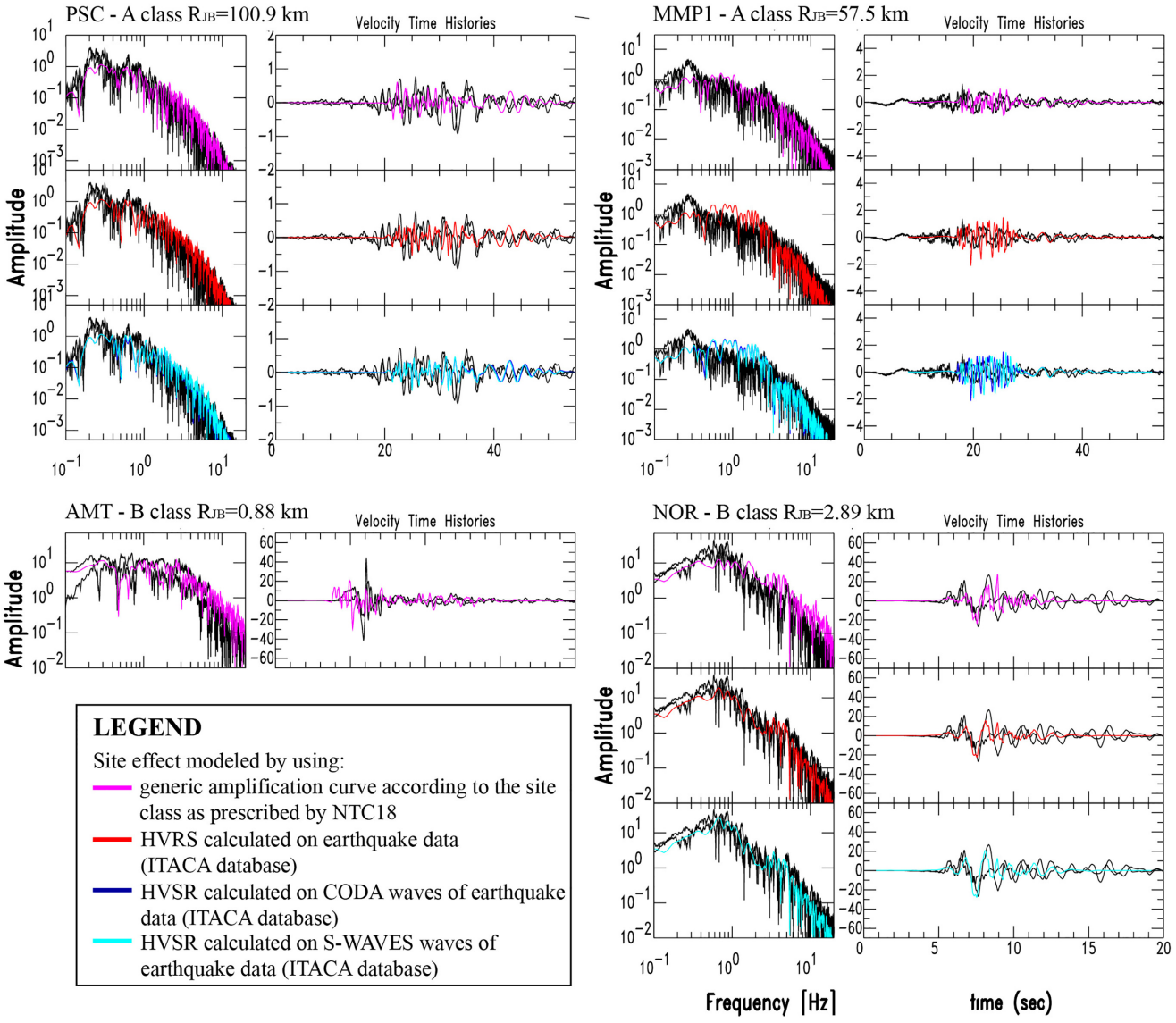

Figure 14. (*Continued.*)

two peaks on HVRSs and HVSRs at 0.3 and 1.6 Hz, with amplitude 5–10. Station AVZ shows a good fit between recorded and simulated ground motion, which increases slightly by using the amplification curve by HVRSs and HVSRs. Conversely, at station BTT2 recorded seismograms highlight the presence of low frequency phases, mostly in the coda, due to 3-D amplification caused by the impedance contrast between soft sediments and underlying rock formations, and by wave reverberation across the sedimentary body.

As 2-D/3-D effects and reverberations at low frequency are observed only in the middle of the basins (i.e. Bard & Bouchon 1998; Moczo *et al.* 1995; Kawase 1996; Gaffet *et al.* 2000; Cornou *et al.* 2003) differences in the capability of our model to reproduce observations at AVZ and BTT2 are due to the different location of the two stations in the sedimentary basin. As for CLF, the observed ground motion was not reproduced at BTT2 since 3-D amplification effects cannot be fully simulated using the stochastic finite-fault approach implemented in this study.

In Fig. 14(b) we show other examples with velocity Fourier spectra and time histories derived from the use of the following amplification curves: the generic amplification curve; the means of HVRSs provided in ITACA database and calculated at each station on earthquake data; the means of HVSRs calculated at each station on coda waves using the earthquake data available in ITACA database for each station; the means of HVSRs calculated on *S* waves (when available). At stations PSC and MMP1, both on rock sites and lying in the site NTC18 class-A, we did not obtain any significant improvement of the fit between observed and simulated when using different amplification curves, since no amplification effects are expected nor observed on HVRSs and HVSRs. Consistently, also at stations AMT and NOR, close to the seismic source, no changes are observed when changing amplification curve, ground motion being dominated by the source effect.

5 CONCLUSIONS

In this study, we investigate whether the physics-based broad-band ground motion simulations can successfully produce the observed ground motions of the Amatrice earthquake.

The general good consistency found between synthetic and observed ground motion (both in the time and frequency domains), suggests that the use of regional specific source scaling and attenuation parameters in hybrid simulations permits to satisfactory reproduce ground motion estimates. Synthetic hybrid waveforms and Fourier amplitude are generally compatible with records, demonstrating that our model can adequately explain spectral amplitudes, temporal characteristics of observed seismograms and to detect near-source effects related to the distribution of asperities on the fault plane. As they are built, these hybrid models include directivity effects only at low frequencies. For this earthquake, we observe that our simulations are not able to fully capture the source-related directivity effects because they are persistent also at higher frequencies ($f > 2$ Hz). Despite the limitations of the adopted approach in simulating the directivity effects, it is attendant that the stochastic finite fault model is a very practical appliance for calculating the ground motion parameters (Atkinson & Assatourians 2015; Goulet *et al.* 2015). Furthermore, it can be easily used both for region-specific and path-specific applications as well as for areas where there are no or few strong motion stations are available.

Finally, we remark that the use of generic amplification curves led at several sites to a mismatch between simulated and observed ground motion, due to an improper consideration of the site contribution in ground motion amplification. By testing the application of HVRS and HVSR specifically and separately calculated at some stations, we have found a general improvement of the fit between simulated and observed ground motion. A limit in the followed approach regards sites affected by 2-D/3-D effects in sedimentary basins, since such reverberations at low frequency cannot be simulated throughout a stochastic model and methods.

We finally stress two important limitations about the parametrization of the site effect. The former is represented by the assignment of the site class considering the outcropping lithology and through inferences on the basis of local geological conditions, rather than by performing *in situ* seismic velocity measurements. This is a common practice since velocity measurements are expensive and time consuming, but often results in incorrect site classification, and therefore in inaccurate site effects estimates and insufficient ground motion amplification. The latter limitation is intrinsic in the Vs_{30}-based soil site classification adopted in the seismic code, which is insensitive to at depth higher than 30 m, and is unable to capture low-frequency peaks produced by impedance contrasts at depths higher than 30 m.

Finally, we acquainted that these results may be improved using more sophisticated simulation methods that consider 3-D structure of the earth including basins and topographic effects as well as the dynamic rupture modelling which will be the further effort in the next step. The data underlying this article are available in the ITACA database (ITalian ACcelerometric Archive, http://itaca.mi.ingv.it/ItacaNet_30/#/home, last accessed October 2020). Many of the plots were generated using the Generic Mapping Tools (http://www.soest.hawaii.edu/gmt, last accessed December 2008, Wessel *et al.* 2013).

ACKNOWLEDGEMENTS

We wish to thank the reviewer Arben Pitarka for his thorough reviews that improved the manuscript. We also thank an anonymous Reviewer and the Editor Eiichi Fukuyama, who provided valuable comments and suggestions that contributed to implement the paper. Research activities were led out within the Seismic Hazard Center (Centro di Pericolosità Sismica) at the INGV. They have been funded by the Presidenza del Consiglio dei Ministri, Dipartimento della Protezione Civile. The authors are responsible of the content of this paper, which does not necessarily reflect the official position and policies of the Department of Civil Protection.

REFERENCES

Amoroso, S., Gaudiosi, I., Tallini, M., Di Giulio, G. & Milana, G, 2018. 2D site response analysis of a cultural heritage: the case study of the site of Santa Maria di Collemaggio Basilica (L'Aquila, Italy), *Bull. Earthq. Eng.,* **16,** 4443.

Anderson, J.G. & Hough, S.R., 1984. A model for the shape of the Fourier amplitude spectrum of acceleration at high frequencies, *Bull. seism. Soc. Am.,* **74**(5), 1969–1993.

Aringoli, A. *et al.*, 2016. The August 24th 2016 Accumoli earthquake: surface faulting and Deep-Seated Gravitational Slope Deformation (DSGSD) in the Monte Vettore area, *Ann. Geophys.,* **59,** Fast Track 5, 2016; doi:10.4401/ag-7199.

Al Atik, L., Abrahamson, N., Bommer, J.J., Scherbaum, F., Cotton, F. & Kuehn, N., 2010. The variability of ground-motion prediction models and its components, *Seismol. Res. Lett.,* **81**(5), 794–801.

Atkinson, G.M. & Boore, D.M., 2006. Earthquake ground-motion prediction equations for eastern North America, *Bull. seism. Soc. Am.,* **96,** 2181–2205.

Akinci, A., Malagnini, L. & Sabetta, F., 2010. Characteristics of the strong ground motions from the 6 April 2009 L'Aquila earthquake, Italy. *Soil Dyn. Earthq. Eng.,* **30**(5), 320–335.

Akinci, A., Aochi, H., Herrero, A., Pischiutta, M. & Karanikas, D., 2017. Physics-based broadband ground-motion simulations for probable Mw ≥7:0 earthquakes in the Marmara Sea Region (Turkey), *Bull. seism. Soc. Am.,* **107**(3), doi: 10.1785/0120160096.

Atkinson, G.M. & Assatourians, K., 2015. Implementation and validation of EXSIM (a stochastic finite-fault ground-motion simulation algorithm) on the SCEC broadband platform. *Seismol. Res. Lett.,* **86**(1), 48–60.

Barchi, M., DeFeyter, A., Magnani, M., Minelli, G., Pialli, G. & Sotera, B., 1998. Extensional tectonics in the Northern Apennines (Italy): evidence from the CROP03 deep seismic reflection line, *Memorie della Societa Geologica Italiana,* **52,** 528–538.

Bard, P-Y & Bouchon, M., 1998. The two-dimensional resonance of sediment-filled valleys, *Bull. seism. Soc. Am.,* **75**(2), 519–541.

Berge, C., Gariel, J.-C. & Bernard, P., 1998. Avery broad-band stochastic source model used for near source strong motion prediction, *Geophys. Res. Lett.,* **25**(7), 1063–1066.

Bindi, D., Pacor, F., Luzi, L., Puglia, R., Massa, M., Ameri, G. & Paolucci, R., 2011. Ground motion prediction equations derived from the Italian strong motion database, *Bull. Earthq. Eng.,* **9**(6), 1899–1920.

Boore, D.M., 2005. SMSIM—Fortran Programs for Simulating Ground Motions from earthquakes: Version 2.3—A Revision of OFR 96–80–A, available at http://www.daveboore.com/smsim.

Boore, D.M., 2009. Comparing stochastic point-source and finite-source ground-motion simulations: SMSIM and EXSIM, *Bull. seism. Soc. Am.,* **99,** 3202–3216.

Boore, D.M. & Joyner, W.B., 1997. Site amplifications for generic rock sites, *Bull. seism. Soc. Am.,* **87,** 327–341.

Boore, D.M., 2016. Determining generic velocity and density models for crustal amplification calculations, with an update of the Boore and Joyner (1997) generic site amplification for VS(30) = 760 m/s, *Bull. seism. Soc. Am.,* **106,** 316–320.

Boore, D.M., 2003. Simulation of ground motion using the stochastic method, *Pure appl. Geophys.,* **160,** 635–676.

Boore, D.M., Stewart, P.J., Seyhan, E. & Atkinson, G.M., 2014. NGAWest2 equations for predicting PGA, PGV, and 5% damped PSA for shallow crustal earthquakes, *Earthq. Spectra,* **30**(3), 1057–1085.

Calderoni, G., Rovelli, A. & Di Giovambattista, R., 2017. Rupture directivity of the strongest 2016–2017 central Italy earthquakes, *J. Geophys. Res.,* **122,** 9118– 9131.

Campbell, K.W. & Boore, D.M., 2016. Evaluation of six NEHRP B/C crustal amplification models proposed for use in Western North America, *Bull. seism. Soc. Am.,* **106,** 673–686.

Cavinato, G.P. & De Celles, P.G., 1999. Extensional basins in the tectonically bimodal central Apennines fold-thrust belt, Italy: response to corner flow above a subducting slab in retrograde motion, *Geology,* **27**(10), 955–958.

Cornou, C., Bard, P-Y. & Dietrich, M., 2003. Contribution of dense array analysis to the identification and quantification of basin-edge-induced waves, Part I: methodology, *Bull. seism. Soc. Am.,* **93**(6), 2604–2623.

De Luca, G., Marcucci, S., Milana, G. & Sanò , T., 2005. Evidence of low frequency amplification in the City of L'Aquila, Central Italy, through a multidisciplinary approach including strong- and weak-motion data, ambient noise, and numerical modeling, *Bull. seism. Soc. Am.,* **95,** 1469–1481.

Di Giulio, G., Gaudiosi, J., Cara, F. & Milana, G., 2014. Shear-wave velocity profile and seismic input derived from ambient vibration array measurements: the case study of downtown L'Aquila, *Geophys. J. Int.,* **198,** 848–866.

Di Giulio, G., Cornou, C., Ohrnberger, M., Wathelet, M. & Rovelli, A., 2006. Deriving wavefield characteristics and shear-velocity profiles from two-dimensional small-aperture arrays analysis of ambient vibrations in a small-size Alluvial Basin, Colfiorito, Italy, *Bull. seism. Soc. Am.,* **96**(5), 1915–1933.

Douglas, J. & Aochi, H., 2008. A survey of techniques for predicting earthquake ground motions for engineering purposes, *Surv. Geophys.,* **29,** 187, doi: 10.1007/s10712-008-9046-y.

Dreger, D.S., Gee, L., Lombard, P., Murray, M.H. & Romanowicz, B., 2005. Rapid finite-source analysis and near-fault strong ground motions: application to the 2003 Mw 6.5 San Simeon and 2004 Mw 6.0 Parkfield earthquakes, *Seismol. Res. Lett.,* **76**(1), 40–48.

EMERGEO Working Group, 2016. Coseismic effects of the 2016 Amatrice seismic sequence: first geological results, *Ann. Geophys.,* **59**(5),.

Falcucci, E., Gori, S., Galadini, F., Fubelli, G., Moro, M. & Saroli, M., 2016. Active faults in the epicentral and mesoseismal Ml 6.0 24, 2016 Amatrice earthquake region, central Italy. Methodological and seismotectonic issues. *Ann. Geophys.,* **59,** Fast Track 5; doi:10.4401/ ag-7266.

Galli, P., Peronace, E. & Tertulliani, A., 2016a. *Rapporto sugli effetti macrosismici del terremoto del 24 agosto 2016 di Amatrice in scala MCS,* Roma, Rapporto congiunto DPC, CNRIGAG, 15pp; doi:10.5281/zenodo.161323.

Galli, P., Peronace, E., Bramerini, F., Castenetto, S., Naso, G., Cassone, F. & Pallone, F., 2016b. The MCS intensity distribution of the devastating 24 August 2016 earthquake in central Italy (M_W 6.2), *Ann. Geophys.,* **59,** doi:10.4401/ag-7287.

Gaffet, S. *et al.*, 2000. A site effect study in the Verchiano valley during the 1997 Umbria-Marche (Central Italy) earthquakes, *J. Seismol.,* **4,** 525–541.

Goulet, C.A., Abrahamson, N.A., Somerville, P.G. & Wooddell, K.E., 2015. The SCEC broadband platform validation exercise: methodology for code validation in the context of seismic hazard analyses, *Seismol. Res. Lett.,* **86**(1), doi:10.1785/0220140104.

Graves, R. & Pitarka, A., 2010. Refinements to the Graves and Pitarka (2010) broadband ground-motion simulation method, *Seismol. Res. Lett.,* **86**(1), 75–80.

Guatteri, M., Mai, P.M. & Beroza, G.C., 2004. A pseudo-dynamic approximation to dynamic rupture models for strong ground motion prediction, *Bull. seism. Soc. Am.,* **94**(6), 2051–2063.

Guatteri, M., Mai, P.M., Beroza, G.C. & Boatwright, J., 2003. Strong ground motion prediction from stochastic-dynamic source models, *Bull. seism. Soc. Am.,* **93**(1), 301–313.

Hartzell, S.H., 1978. Earthquake aftershocks as Green's functions, *Geophys. Res. Lett.,* **5,** 1–4.

Hartzell, S., Harmsen, S.C., Frankel, A.D. & Larsen, S., 1999. Calculation of broadband time histories of ground motion; comparison of methods and validation using strong-ground motion from the 1994 Northridge earthquake, *Bull. seism. Soc. Am.,* **90**(6), 1484–1504.

Hartzell, S., Guattieri, M., Mai, M., Liu, P.-C. & Fisk, M., 2005. Calculation of broadband time histories of ground motion, Part II: kinematic and dynamic modeling using theoretical Green's functions and comparison with the 1994 Northridge earthquake, *Bull. seism. Soc. Am.,* **95**(2), 614–645.

Herrmann, R.B., Malagnini, L. & Munafò, I., 2011. Regional moment tensor of the 2009 L'Aquila earthquake sequence, *Bull. seism. Soc. Am.,* **101**(3), 975–993.

Herrero, A. & Bernard, P., 1994. A kinematic self-similar rupture process for earthquakes, *Bull. seism. Soc. Am.,* **84**(4), 1216–1228.

Irikura, K. & Miyake, H., 2011. Recipe for predicting strong ground motion from crustal earthquake scenarios, *Pure appl. Geophys.,* **168,** 85–104.

Irikura, K., 1986. Prediction of strong acceleration motion using empirical Green's function, in *Proceedings of the 7th Japan Earthq. Eng. Symposium*.

ISIDe Working Group (INGV), 2016. *Italian seismological instrumental and parametric database*: http://iside.rm.ingv.it, (last accessed September 2016), doi: 10.13127/ISIDe.

Kawase, H., 1996. The cause of the damage belt in Kobe: "The Basin-Edge Effect," constructive interference of the direct S-wave with the basin-induced diffracted Rayleigh waves, *Seismol. Res. Lett.,* **67**(5), 25–34.

Lanzano, G., Luzi, L., Pacor, F., Puglia, R., D'Amico, M., Felicetta, C. & Russo, E., 2016. Preliminary analysis of the accelerometric recordings of the August 24th, 2016 MW 6.0 Amatrice earthquake, *Ann. Geophys.,* **59,** Fast Track 5, 2016 doi:10.4401/ag-7201

Lavecchia, G., Brozzetti, F., Barchi, M., Menichetti, M. & Keller, J.V., 1994. Seismotectonic zoning in east-central Italy deduced from an analysis of the Neogene to present deformations and related stress fields, *Bull. geol. Soc. Am.,* **106**(9), 1107–1120.

Liu, P.C., Archuleta, R.J. & Hartzell, S.H., 2006. Prediction of broadband ground-motion time histories: Hybrid low/high-frequency method with correlated random source parameters, *Bull. seism. Soc. Am.,* **96**(6), 2118–2130.

Luzi, L. *et al.*, 2017. The Central Italy seismic sequence between August and December 2016: analysis of strong motion observations. *Seism. Res. Lett.,* **88**(5), 1219–1231.

Mai, P.M. & Beroza, G.C., 2003. A hybrid method for calculating near source, broadband seismograms: application to strong motion prediction, *Phys. Earth Planet. Inter.,* **137,** nos. 1/4, 183–199.

Mai, P.M., Imperatori, W. & Olsen, K.B., 2010. Hybrid broadband ground motion simulations: combining long-period deterministic synthetics with high-frequency multiple S-to-S backscattering, *Bull. seism. Soc. Am.,* **100**(5A), 2124–2142.

Malagnini, L., Akinci, A., Mayeda, K., Munafo, I., Herrmann, R.B. & Mercuri, A., 2011. Characterization of earthquake-induced ground motion from the L'Aquila seismic sequence of 2009, Italy, *Geophys. J. Int.,* **184,** 325–337.

Mena, B., Dalguer, L.A. & Mai, P.M., 2012. Pseudodynamic source characterization for strike-slip faulting including stress heterogeneity and supershear ruptures, *Bull. seism. Soc. Am.,* **102**(4), 1654–1680.

Moczo, P., Rovelli, A., Labàk, P. & Malagnini, L., 1995. Seismic response of the geologic structure underlying the Roman Colosseum and a 2.D resonance of a sediment valley, *Annali di geofisica,* **28,** 939–956.

Motazedian, D. & Atkinson, G.M., 2005. Stochastic finite-fault modelling based on a dynamic corner frequency, *Bull. seism. Soc. Am.,* **95,** 995–1010.

NTC18, Italian building code 'Norme Tecniche per le Costruzioni – Ministero delle Instrutture e dei Trasporti, 2018. https://www.gazzettaufficiale.it/eli/gu/2018/02/20/42/so/8/sg/pdf, (last accessed December 2020).

Pischiutta, M., Akinci, A., Malagnini, L. & Herrero, A., 2016. Characteristics of the strong ground motion from the 24th August 2016 Amatrice Earthquake, *Ann. Geophys.,* **59,** Fast Track 5.

Pitarka, A., Graves, R., Irikura, K., Miyakoshi, K. & Rodgers, A., 2019. Kinematic rupture modeling of ground motion from the M7 Kumamoto, Japan, Earthquake. *Pure appl. Geophys.,* **177,** 2199–2221.

Pitarka, A., Graves, R., Irikura, K., Miyake, H. & Rodgers, A., 2017. Performance of Irikura recipe rupture model generator in earthquake ground motion simulations with graves and Pitarka hybrid approach, *Pure appl. Geophys.,* **174**(9), 3537–3555.

Pucci, S. *et al.*, 2017. Coseismic ruptures of the 24 August 2016, Mw 6.0 Amatrice earthquake (central Italy), *Geophys. Res. Lett.,* **44,** 2138–2147.

Puglia, R., Ditommaso, R., Pacor, F., Mucciarelli, M., Luzi, L. & Bianca, M., 2011. Frequency variation in site response as observed from strong motion data of the L'Aquila (2009) seismic sequence, *Bull. Earthq. Eng.,* **9,** 869.

Quest, W.G., 2016. The 24 August 2016 Amatrice earthquake: macroseismic survey in the damage area and EMS intensity assessment, *Ann. Geophys.,* **59,** fast track 5, 2016; doi:10.4401/ag-7203

Ren, Y., Wang, H. & Wen, R., 2017. Imprint of rupture directivity from ground motions of the 24 August 2016 Mw6.2 Central Italy earthquake, *Tectonics,* **36,** 3178–3191.

Ross, Z.E., Trugman, D.T., Azizzadenesheli, K. & Anandkumar, A., 2020. Directivity modes of earthquake populations with unsupervised learning, *J. geophys. Res.,* **125,** doi:10.1029/2019JB018299.

Saragoni, G.R. & Hart, F.C., 1974. Simulation of artificial earthquake accelerograms, *J. Earthq. Eng. Struct. Dyn.,* **2,** 249–267.

Schmedes, J. & Archuleta, R.J., 2008. Near-source ground motion along strike-slip faults: Insights into magnitude saturation of PGV and PGA, *Bull. seism. Soc. Am.,* **98**(5), 2278–2290.

Schmedes, J., Archuleta, R.J. & Lavallée, D., 2010. Correlation of earthquake source parameters inferred from dynamic rupture simulations, *J. geophys. Res.,* **115,** doi:10.1029/2009JB006689.

Somerville, P.G., 2003. Magnitude scaling of the near fault rupture directivity pulse, *Phys. Earth planet. Inter.,* **137,** 201–212.

Song, S.G., Dalguer, L.A. & Mai, P.M., 2014. Pseudo-dynamic modelling with 1-point and 2-point statistics of earthquake source parameters, *Geophys. J. Int.,* **196,** 1770–1786.

Spagnuolo, E., Cirella, A. & Akinci, A., 2016. Investigating the effectiveness of rupture directivity during the Mw 6.0 Amatrice earthquake, central Italy, *Ann. Geophys.,* **59,** Fast Track 5, 2016.

Tinti, E., Scognamiglio, L., Michelini, A. & Cocco, M. 2016. Slip heterogeneity and directivity of the ML 6.0, 2016, Amatrice earthquake estimated with rapid finite-fault inversion, *Geophys. Res. Lett.,* **43,** 10745–10752.

Ugurhan, B., Askan, A., Akinci, A. & Malagnini, L., 2010. Strong ground motion simulation of the 6 April 2009 L'Aquila, Italy, Earthquake, *Bull. seism. Soc. Am.,* **102**(4), 1429–1445.

Wessel, P., Smith, W.H.F., Scharroo, R., Luis, J. & Wobbe, F., 2013. Generic Mapping Tools: Improved Version Released, EOS Trans, *EOS Trans. AGU,* **94**(45), p. 409–410, doi:10.1002/2013EO450001, (last accessed December 2020).

Zanini, M.A., Hofer, L., Faleschini, F., Zampieri, P., Fabris, N. & Pellegrini, C., 2016, Preliminary macroseismic survey of the 2016 Amatrice seismic sequence, *Ann. Geophys.,* **59,** Fast Track 5; doi:10.4401/ag-7172.za.

SUPPORTING INFORMATION

Supplementary data are available at *GJI* online.

SUPPL_MAT_4publ.zip

Please note: Oxford University Press is not responsible for the content or functionality of any supporting materials supplied by the authors. Any queries (other than missing material) should be directed to the corresponding author for the paper.